

# Computing committers via Mahalanobis diffusion maps with enhanced sampling data

L. Evans,<sup>1, a)</sup> M.K. Cameron,<sup>1, b)</sup> and P. Tiwary<sup>2, c)</sup>

<sup>1)</sup>*Department of Mathematics, University of Maryland, College Park, MD 20742, USA*

<sup>2)</sup>*Department of Chemistry and Biochemistry and Institute for Physical Science and Technology, University of Maryland, College Park, MD 20742, USA*

(\*Electronic mail: ptiwary@umd.edu)

(\*Electronic mail: mariakc@umd.edu)

(\*Electronic mail: evansal@umd.edu)

(Dated: 31 August 2022)

The study of phenomena such as protein folding and conformational changes in molecules is a central theme in chemical physics. Molecular dynamics (MD) simulation is the primary tool for the study of transition processes in biomolecules, but it is hampered by a huge timescale gap between the processes of interest and atomic vibrations which dictate the time step size. Therefore, it is imperative to combine MD simulations with other techniques in order to quantify the transition processes taking place on large timescales. In this work, the diffusion map with Mahalanobis kernel, a meshless approach for approximating the Backward Kolmogorov Operator (BKO) in collective variables, is upgraded to incorporate standard enhanced sampling techniques such as metadynamics. The resulting algorithm, which we call the *target measure Mahalanobis diffusion map* ( $\tau_m$ -mmap), is suitable for a moderate number of collective variables in which one can approximate the diffusion tensor and free energy. Imposing appropriate boundary conditions allows use of the approximated BKO to solve for the committor function and utilization of transition path theory to find the reactive current delineating the transition channels and the transition rate. The proposed algorithm,  $\tau_m$ -mmap, is tested on the two-dimensional Moro-Cardin two-well system with position-dependent diffusion coefficient and on alanine dipeptide in two collective variables where the committor, the reactive current, and the transition rate are compared to those computed by the finite element method (FEM). Finally,  $\tau_m$ -mmap is applied to alanine dipeptide in four collective variables where the use of finite elements is infeasible.

## I. INTRODUCTION

Molecular dynamics (MD) simulations provide an atomistic-resolution lens for probing chemical systems. These systems commonly have high dimensionality, reside in metastable states on extremely large time scales, and undergo transitions on extremely small time scales relative to residence times in the metastable states. These transitions, such as protein folding or conformational changes in a molecule, are crucial to molecular simulations but difficult to characterize due to the timescale gap, and are thus commonly referred to as rare events. The transition path theory (TPT)<sup>1-3</sup> is a mathematical framework for the direct study of such rare transitions in stochastic systems, and it is particularly utilized for metastable systems arising in MD. TPT is framed around the committor function, an optimal reaction coordinate with which reaction rates and reaction channels can be computed between a predefined reactant state  $A$  and product state  $B$ . In practice, the committor is very difficult to compute globally: statistical or simulation-based methods require observing large numbers of rare transitions while mathematical partial differential equation (PDE)-based approaches require gridding the state space and thus are limited to low dimensions. Instead, numerical TPT for high-dimensional

systems typically involves finding a zero-temperature asymptotic transition path and using umbrella sampling or related techniques to access the committor.<sup>2</sup> This approach is viable but assumes that rare transitions are localized to a narrow tube around the found path. In practice, transition processes can be broad and complex<sup>4</sup> and the computed path may misrepresent the true kinetics.

For a more global analysis one can instead utilize collective variables to lower the dimensionality and increase interpretability of existing methods.<sup>5,6</sup> However, a biomolecule may still require a large number of collective variables such as contact distances or dihedral angles for adequate representation.<sup>7-10</sup> Hence, one still may be unable to leverage traditional mesh-based PDE solvers to even reduced dimensionality data given either in physics-informed or machine-learned collective variables.

In contrast to traditional PDE solvers, meshless approaches to computing the committor discretize the backward Kolmogorov PDE to a point cloud obtained from a molecular dynamics simulation. Recent approaches of this type include parametrizing the committor with a neural network<sup>11-14</sup> and approximating dynamical operators with diffusion maps.<sup>15,16</sup>

The diffusion map algorithm introduced by Coifman and Lafon<sup>17</sup> in 2006 is a widely used dimension reduction algorithm which provably approximates differential operators on unstructured datasets. Its extensions most relevant to the present work include several works concerning the sampling and transformation of the input data. The Mahalanobis diffusion map<sup>18</sup> untangles the effect of nonlinear transforma-

<sup>a)</sup><https://www.math.umd.edu/~evansal/>

<sup>b)</sup><http://www.math.umd.edu/~mariakc/>

<sup>c)</sup><https://go.umd.edu/tiwarylab>

tion applied to the data. Integration with umbrella sampling<sup>19</sup> uncovers informative low-dimensional local parametrizations for the high-dimensional system of interest. Local kernels<sup>20</sup> adapt diffusion maps for data coming from processes governed by arbitrary Ito SDEs. The *target measure diffusion map*<sup>15,21</sup> allows for the data to be sampled from an arbitrary density provided that the invariant density for the process of interest is known.

The original diffusion map algorithm<sup>17</sup> relies on the assumption that the input data are sampled from a Gibbs distribution of interest and that the underlying process is governed by the overdamped Langevin dynamics. It constructs an approximation to the backward Kolmogorov operator (the generator) using only the input data – no additional information about the process is needed. Central to this construction is the kernel function serving as a proximity function between the data points. Usually it is chosen to be the standard rotationally symmetric Gaussian function with the bandwidth parameter tuned by the user. The kernel function evaluated on each pair of data points is converted to a generator matrix for a discrete-time Markov chain with the data points comprising its set of states. The dynamics of this Markov chain approximates the dynamics of the system governed by the overdamped Langevin dynamics whose invariant density is the sampling density for the data points<sup>17</sup>. In our recent work<sup>16</sup>, the diffusion map algorithm was promoted to approximate the dynamics in collective variables that is time-reversible but may have a position-dependent and anisotropic diffusion tensor. This version featured the Mahalanobis kernel<sup>18</sup> and required the calculation of the diffusion tensor in collective variables at each data point by umbrella sampling<sup>6</sup>. We proved rigorously that the resulting Mahalanobis diffusion map (mmap) accurately approximates the generator in collective variables and numerically validated the algorithm on simple MD systems.<sup>16</sup>

In this work, we extend mmap<sup>16</sup> to work with input data generated by any standard enhanced sampling technique. Remarkably, *knowledge of the sampling density is not required*. A reweighting scheme for the rotationally symmetric Gaussian kernel making it capable of taking data from an arbitrary sampling density was proposed by Banisch et al.<sup>15,21</sup> Here we modify this reweighting scheme for the Mahalanobis kernel and offer a convergence proof. We will refer to the resulting algorithm as the *target measure Mahalanobis diffusion map* and abbreviate it as tm-mmap.

It is important to note that for metastable molecular systems quantities like the committer are relevant precisely where sampling is extremely difficult. Enhanced sampling approaches such as umbrella sampling<sup>22</sup> and metadynamics<sup>23</sup> can alleviate this issue. The proposed algorithm, tm-mmap, combines mmap with the enhanced sampling. Its output is the committer function that is processed via the transition path theory to obtain the reactive current and the transition rate between the metastable states of interest. In sum, tm-mmap is a simple and customizable tool which expands the diffusion map framework to user-defined coordinates and sampling for rare event analysis in molecular dynamics.

We validate tm-mmap on the Moro-Cardin two-well system

with position-dependent diffusion<sup>24</sup> and on alanine dipeptide with two dihedral angles in vacuum. Here metadynamics<sup>23</sup> is used for enhanced sampling, though our method could easily work in conjunction with other enhanced sampling approaches. We compare the tm-mmap committer, the reactive current, and the transition rate to those computed using the finite element method and show that the tm-mmap committers and rates are robust with respect to the choice of the kernel bandwidth. Of particular note for practical interest is that the kernel bandwidth values chosen from a standard heuristic<sup>25–28</sup> achieve near-optimal error for the committer on a variety of subsampled datasets, particularly for quasi-uniformly subsampled data.

Finally, we apply tm-mmap to alanine dipeptide with four dihedral angles in vacuum and demonstrate its ability to facilitate the quantification of the transition process between the C7eq and C7ax metastable states in 4D. Moreover, the transition rate computed for this transition using tm-mmap is in good agreement with the estimate obtained by simulating a very long unbiased trajectory in Ref. 29.

The rest of the paper is organized as follows. Background on the Langevin dynamics, collective variables, the transition path theory, and diffusion maps is given in Section II. The proposed methodology including the tm-mmap algorithm as well as algorithms for choosing parameters and processing input data are detailed in Section III. Numerical tests are presented in Section IV. An application to alanine dipeptide in four dihedral angles is reported in Section V. A discussion of the results is found in Section VI. Conclusions are summarized in Section VII. A convergence proof for tm-mmap is placed in Appendix B.

## II. BACKGROUND

### A. Effective Dynamics in Collective Variables

Our primary interest in this work is in datasets arising in MD simulations, though we believe the formalism developed here would be applicable to generic trajectories across chemical physics obtained from simulations or experiments. We consider the *Langevin dynamics*, a commonly used model for molecular motion which describes the molecular configuration in terms of the atomic positions  $y$  and their velocities  $v$ :

$$dy = vdt \quad (1)$$

$$dv = -(m^{-1}\nabla V(y) + \gamma v) dt + \sqrt{2\gamma(m\beta)^{-1}}dw. \quad (2)$$

Here  $V : \mathbb{R}^n \rightarrow \mathbb{R}$  is a potential function,  $\beta^{-1} = k_b T$  is temperature in units of Boltzmann’s constant,  $t$  is time,  $\gamma$  is the friction coefficient,  $m$  is the diagonal  $n \times n$  mass matrix, and  $w_t$  is a Brownian motion in  $\mathbb{R}^n$ . We assume that the potential  $V(y)$  is such that the system governed by (1) is ergodic with respect to the invariant Boltzmann-Gibbs density

$$\mu(y, v) = Z_y^{-1} (2\pi)^{-n/2} m^{1/2} \exp \left\{ -\beta \left( V(y) + \frac{1}{2} v^\top m v \right) \right\},$$

where  $Z_y$  is a normalizing constant.

As mentioned in the Introduction, the number of atoms in biomolecules is typically very large. Even the small molecule alanine dipeptide has 22 atoms, and hence has a 66-dimensional configuration space ( $n = 66$ ) and 132-dimensional phase space  $(y, v)$ . On the other hand, an effective description of the state of a biomolecule is usually done in terms of certain functions in  $y$  specifying desired geometric characteristics rather than in terms of  $(y, v)$ . Therefore, to reduce the dimensionality and obtain a more useful and comprehensive description of the system-at-hand, one uses *collective variables* (CVs). CVs are functions of the atomic coordinates designed to give a coarse-grained description of the system's dynamics, preserving transitions between metastable states but erasing small-scale vibrations. Physical intuition has traditionally driven the choice of collective variables including dihedral angles, intermolecular distances, macromolecular distances and various experimental measurements.

For a given system configuration  $y \in \mathbb{R}^n$ , we denote the CV coordinates at  $y$  as  $\theta(y) = (\theta_1(y), \dots, \theta_d(y))^\top \in \Omega$  where  $d \ll n$  and  $\Omega$  is a  $d$ -dimensional manifold whose local geometry coincides with  $\mathbb{R}^d$ , or is simply  $\mathbb{R}^d$ . For all practical purposes, the space of collective variables is  $\Omega = \mathbb{R}^k \times \mathbb{T}^{d-k}$  where  $k$  is any integer satisfying  $0 \leq k \leq d$ .

We assume that  $\theta(y)$  is a sufficiently ‘good’ set of CVs (given more precisely in Section II.B) such that we can describe a closed dynamics in coordinates  $x = \theta(y)$  by the anisotropic overdamped Langevin dynamics of the form<sup>6</sup>

$$dx_t = (-M(x_t)\nabla F(x_t) + \beta^{-1}\nabla \cdot M(x_t))dt + \sqrt{2\beta^{-1}M^{1/2}(x_t)}dW_t, \quad (3)$$

where  $F(x)$  is the *free energy* with respect to the CVs given by

$$F(x) = -\beta^{-1} \ln \left( \int_{\mathbb{R}^n} Z_y^{-1} e^{-\beta V(y)} \delta(\theta(y) - x) dy \right), \quad (4)$$

and  $M(x)$  is the *diffusion matrix* for the CVs defined by

$$M(x) = e^{\beta F(x)} \int_{\mathbb{R}^n} J(y)mJ^\top(y)Z_y^{-1} e^{-\beta V(y)} \delta(\theta(y) - x) dy. \quad (5)$$

Here  $J(y)$  is the  $d \times n$  Jacobian matrix with entries

$$J_{ij}(y) = \frac{\partial \theta_i(y)}{\partial y_j} \quad 1 \leq i \leq d, \quad 1 \leq j \leq n.$$

Note that since the collective variables depend only on the positions  $y$ , the velocities  $v$  are integrated out in deriving the effective dynamics (3).

One can check that the invariant probability measure for the process governed by SDE (3) is the Gibbs density

$$\rho(x) = Z_x^{-1} e^{-\beta F(x)}, \quad (6)$$

and that the process is time-reversible<sup>2</sup>. Moreover, any reversible diffusion process must be of the form (3) for some function  $F(x)$  and some matrix  $\beta^{-1}M(x)$ . The drift term

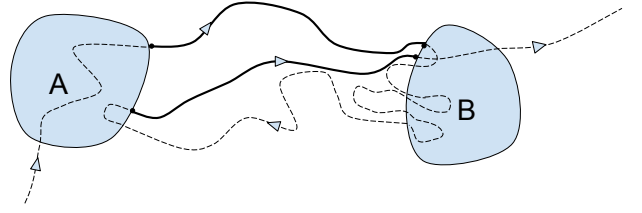


**FIG. 1:** A segment of a long trajectory. Reactive pieces from reactant state  $A$  to product state  $B$  are shown with solid lines.

$\beta^{-1}\nabla \cdot M(x)$  is the correction that ensures reversibility.<sup>30</sup> It is a column vector whose  $i$ th component is

$$\beta^{-1}[\nabla \cdot M(x)]_i = \beta^{-1} \sum_{j=1}^d \frac{\partial M_{ij}(x)}{\partial x_j} \quad 1 \leq i \leq d.$$

For the datasets considered in this work, we compute the diffusion matrix  $M(x)$  via local simulations with quadratic position restraints as described in Ref. 6. This procedure is an outgrowth of well-established uses for restrained dynamics within the molecular dynamics community, particularly in position-dependent friction<sup>31</sup> as well as fundamental works for computing free energy differences.<sup>32,33</sup>

The generator for the SDE (3) is given by

$$\mathcal{L}f = (-M\nabla F + \beta^{-1}(\nabla \cdot M))^\top \nabla f + \beta^{-1} \text{tr}[M\nabla \nabla f], \quad (7)$$

which can also be written in divergence form as

$$\mathcal{L}f = \beta^{-1} e^{\beta F} \nabla \cdot (e^{-\beta F} M \nabla f). \quad (8)$$

## B. Transition Path Theory

Let  $\{x_t\}_{t=0}^\infty$  be an infinite trajectory of a system evolving according to SDE (3). We are interested in transitions between disjoint neighborhoods  $A$  and  $B$  of minima  $x_A$  and  $x_B$  of the potential function  $F(x)$ . The sets  $A$  and  $B$  are referred to as the *reactant* and *product* sets respectively. Transition path theory (TPT)<sup>2,3</sup> is a mathematical framework to analyze statistics of transitions between the reactant  $A$  and the product  $B$ . The subject of TPT is the ensemble of *reactive trajectories*, i.e. continuous pieces of the trajectory  $x_t$  which start at  $\partial A$  and end at  $\partial B$  without returning to  $\partial A$  in-between (see Figure 1). Key concepts of TPT are the *forward committor* and *backward committor* functions with respect to  $A$  and  $B$ . Since the governing SDE (3) is reversible, the forward  $q_+$  and backward  $q_-$  committors are related via<sup>2</sup>  $q_- = 1 - q_+$ . Hence, for brevity, we will refer to the forward committor as *the committor* and denote it by  $q(x)$ . The committor  $q$  has a straightforward probabilistic interpretation:

$$q(x) = \mathbb{P}(\tau_B < \tau_A \mid x_0 = x), \quad (9)$$

where  $\tau_A := \inf\{t > 0 \mid x_t \in A\}$  and  $\tau_B := \inf\{t > 0 \mid x_t \in B\}$  are the *first entrance times* of the sets  $A$  and  $B$  respectively. In

words,  $q(x)$  is the probability that a trajectory starting at  $x$  will arrive at the product set  $B$  before arriving at the reactant set  $A$ .

One can show that  $q$  satisfies the boundary value problem<sup>2</sup>

$$\begin{cases} \mathcal{L}q(x) = 0 & x \in \Omega \setminus (A \cup B), \\ q(x) = 0 & x \in \partial A, \\ q(x) = 1 & x \in \partial B, \end{cases} \quad (10)$$

where  $\mathcal{L}$  is the infinitesimal generator from equation (7).

Although the committor can be considered an optimal reaction coordinate,<sup>34,35</sup> the committor by itself does not illustrate the mechanism of the transition process. Instead, from the committor one can compute the *reactive current*, a vector field defined by

$$\mathcal{J} = \beta^{-1} Z_x^{-1} e^{-\beta F(x)} M(x) \nabla q(x). \quad (11)$$

The reactive current gives a complete quantitative characterization of the transition process from  $A$  to  $B$ . Using it, one can identify reactive channels and compute the reaction rates. The integral of the flux of the reactive current through any hypersurface  $\Sigma$  separating the sets  $A$  and  $B$  gives the reaction rate:

$$\nu_{AB} := \lim_{t \rightarrow \infty} \frac{N_{AB}}{t} = \int_{\Sigma} \mathcal{J} \cdot \hat{n} d\sigma, \quad (12)$$

where  $N_{AB}$  is the total number of transitions from  $A$  to  $B$  performed by the system within the time interval  $[0, t]$ , and  $\hat{n}$  is the unit normal to the surface  $\Sigma$  pointing in the direction of  $B$ .

Another quantity of interest is the probability density of reactive trajectories  $\pi_{AB}(x)$ , defined by

$$\pi_{AB}(x) = Z_x^{-1} e^{-\beta F(x)} q(x) (1 - q(x)),$$

which is the probability density to observe a reactive trajectory at  $x \notin (A \cup B)$  at time  $t$ . Note that

$$\rho_{AB} := \int_{\Omega} \pi_{AB} dx \quad (13)$$

is the probability that an infinite trajectory  $x_t$  is reactive at any randomly picked moment of time  $t$ .

Since our goal is to compute the committor and related quantities, our criterion for a good set of good CVs is determined by how well the committor for SDE (3) approximates the committor for the Langevin dynamics (1). We are mostly concerned with a good approximation for the committor in the region of the phase space  $(y, v)$  where the density of reactive trajectories is substantial. Hence, we say that a set of CVs  $y$  is good if the integral

$$\int_{\mathbb{R}^{2n}} |q(\theta(y)) - q(y, v)| \tilde{\pi}_{\tilde{A}\tilde{B}}(y, v) dy dv, \quad (14)$$

is small, where the ‘‘lifted’’ reactant and product sets are defined as  $\tilde{A} := \{(y, v) \mid \theta(y) \in A, \|v\| < r\}$ ,  $\tilde{B}$  likewise, and  $\tilde{\pi}_{AB}(y, v)$  is the probability density of reactive trajectories in the original variables  $(y, v)$ . This criterion is essentially used when the committor is checked by *committor analysis*.<sup>36</sup>

### C. Diffusion Maps

Diffusion maps, like spectral clustering<sup>37</sup> and Laplacian eigenmaps,<sup>38</sup> impose an affinity or similarity measure on a dataset defined by a kernel function, and then analyze the associated graph on the dataset. One interpretation of diffusion maps is that a particular Markov Chain is defined on the data, and analysis of the Markov chain reveals additional structure about the data. An important difference between diffusion maps and previous algorithms, in particular Laplacian eigenmaps<sup>38</sup>, is the emphasis on the discrete-to-continuous interplay of the kernel matrix and algorithmic utilization of known asymptotic error results. Perhaps most important is that the random-walk graph Laplacian on a dataset with sampling density  $\rho(x)$  corresponds to an overdamped Langevin dynamics with stationary measure  $\rho^2(x)$  instead of  $\rho(x)$ . Thus, for non-uniform densities such as a Gibbs distribution, graph Laplacian-like methods must account for the sampling density to obtain correct estimates. Coifman and Lafon<sup>17</sup> in introducing diffusion maps tune the sampling so that for any choice of scalar parameter  $\alpha$  the diffusion map corresponds to a gradient dynamics with stationary density  $\rho^{2(1-\alpha)}$ .

The diffusion map algorithm takes as input a dataset  $X = \{x_i\}_{i=1}^N \subset \mathbb{R}^d$  with sampling density  $\rho(x)$ . For application to molecular dynamics  $x_i$  is usually a vector representing the  $i$ -th molecular conformation from a trajectory, but can generally be considered as a  $d$ -dimensional feature vector for the  $i$ -th piece of data. Pairwise similarity of data is encoded through a distance function  $d(x, x')$  and kernel function  $k_{\varepsilon}(x, x')$ , whose simplest form is given by

$$k_{\varepsilon}(x, x') = \exp\left(-\frac{d(x, x')^2}{2\varepsilon}\right). \quad (15)$$

For many applications  $d(x, x')$  can be taken as Euclidean distance between the vectors  $x, x'$ , but many other distances can be used.<sup>39,40</sup> For datasets consisting of molecular configurations in atomic coordinates, the most commonly used distance is the root-mean-square deviation (RMSD) between configurations.<sup>41,42</sup> Other distances include Euclidean distance after RMSD-aligning configurations to a reference structure<sup>15,43</sup> and hybrid RMSD-energy based distances,<sup>44</sup> with others compared in Ref. 40 as structural and kinetic similarity measures.<sup>45</sup>

The user-chosen parameter  $\varepsilon > 0$  is the *kernel bandwidth*. The kernel defines an  $N \times N$  similarity matrix  $K_{\varepsilon}$  with  $[K_{\varepsilon}]_{ij} = k_{\varepsilon}(x_i, x_j)$ . We can then consider a graph on  $i$  nodes with feature vectors  $X$  and weighted adjacency matrix given by  $K_{\varepsilon}$ . Our goal is to use the discrete graph defined by our data  $X$  and the kernel matrix  $K_{\varepsilon}$  to analyze the continuous process generating the data.

The discrete-to-continuous interplay arises from Monte Carlo integration: for an observable  $f(x)$  and for a sufficiently large dataset with sampling density  $\rho(x)$ ,  $\frac{1}{N} [K_{\varepsilon} f]_i$  is the Monte Carlo approximation for the average of  $k_{\varepsilon}(x_i, \cdot) f(\cdot)$



with respect to  $\rho(x)$  :

$$\lim_{n \rightarrow \infty} \frac{1}{N} \sum_{j=1}^N k_\varepsilon(x_i, x_j) f(x_j) = \int_{\Omega} k_\varepsilon(x_i, x') f(x') \rho(x') dx' \quad (16)$$

with error decaying as  $O(N^{-\frac{1}{2}})$ .

If the dataset comes from an ergodic trajectory with  $x_i$  sampled at timestep  $i$ , we can equivalently interpret the matrix-vector product as a trajectory average with limit

$$\lim_{n \rightarrow \infty} \frac{1}{N} \sum_{j=1}^N k_\varepsilon(x_i, x_j) f(x_j) = \lim_{T \rightarrow \infty} \frac{1}{T} \int_0^T k_\varepsilon(x_i, x_t) f(x_t) dt \quad (17)$$

We define a normalizing factor  $c_\varepsilon(x)$  for a kernel  $k_\varepsilon(x, y)$  as:

$$c_\varepsilon(x) := \int_{\Omega} k_\varepsilon(x, x') dx'. \quad (18)$$

In particular, for the Gaussian kernel with the Euclidean distance and  $\Omega = \mathbb{R}^d$ , the normalizing factor is  $c_\varepsilon = (2\pi\varepsilon)^{d/2}$ .

### 1. Density Estimation

A natural interpretation of the Monte Carlo integration with the kernel  $k_\varepsilon(x, y)$  given by (15) suggests that

$$\frac{1}{c_\varepsilon(x)} k_\varepsilon(x, x') \approx \delta(x - x') \quad (19)$$

for small  $\varepsilon$ . This implies that

$$\frac{1}{c_\varepsilon(x)} \int_{\Omega} k_\varepsilon(x, x') f(x') \rho(x') dx' \approx f(x) \rho(x). \quad (20)$$

Therefore, choosing  $f(x) \equiv 1$ , we can approximate the sampling density  $\rho(x)$  for sufficiently small  $\varepsilon$ . Motivated by this, we define the kernel density estimator  $p_\varepsilon \in \mathbb{R}^N$  as

$$[p_\varepsilon]_i = \frac{1}{N c_\varepsilon(x_i)} \sum_{j=1}^N k(x_i, x_j). \quad (21)$$

At a given node  $x$ , we think of  $K_\varepsilon f$  as a local average or convolution of the observable  $f$  at the node  $x$ , weighted by the kernel function  $k_\varepsilon(x, x')$ . For smaller  $\varepsilon$ , the average will be over a smaller set of neighbors of  $f$ , until  $k_\varepsilon(x, x')$  approaches a  $\delta$ -function.

### 2. Approximating differential operators

A crucial use of the kernel function  $k_\varepsilon(x, y)$  in diffusion maps is for computing derivatives without gridding the phase space. Using Taylor expansions in  $\varepsilon$  and Gaussian integrals, one can compute the error expansion up to second order in  $\varepsilon$  as

$$\frac{1}{c_\varepsilon(x)} \int_{\Omega} k_\varepsilon(x, x') f(x') dx' = f(x) + \frac{\varepsilon}{2} \Delta f(x) + O(\varepsilon^2), \quad (22)$$

where  $\Delta$  denotes the Laplace operator. Note that the left-hand side of (22) is approximated by  $N^{-1} \sum_j k_\varepsilon(x, x_j) f(x_j)$  if the sampling density is uniform in a large enough ball centered at  $x$ . In this case,

$$\Delta f(x_i) \approx \frac{2}{\varepsilon N c_\varepsilon(x_i)} \left[ \sum_{j=1}^N k_\varepsilon(x_i, x_j) f(x_j) - f(x_i) \right]. \quad (23)$$

Note that the Laplacian is the generator corresponding to Brownian motion.

By introducing extra renormalization operations to the kernel matrix, one can obtain approximations to generators for more complicated diffusion processes and for data sampled from an arbitrary density.<sup>15–17,21</sup>

### 3. Target Measure Diffusion Map

In order to quantify rare transitions between metastable regions using the TPT framework, one needs to approximate the generator of the process within the reactive channels and solve the committor boundary value problem (10). Hence, it is necessary to collect data there. This is typically done using *enhanced sampling*: sampling an auxiliary dynamics where rare events are no longer rare. Diffusion maps is a powerful but sampling-dependent method, and enhanced sampling techniques are needed to fuse the algorithm with meaningful study of rare events in molecular simulations. One natural solution is to choose a distribution that is easier to sample, e.g from a higher temperature system<sup>46,47</sup> or from a ‘flat’ energy landscape,<sup>48</sup> and then reweight to a *target measure*  $\mu(x)$ . This reweighting is the idea of *importance sampling* for Monte Carlo integration, and also the foundation of umbrella sampling,<sup>22</sup> one of the oldest enhanced sampling methods.

The target measure diffusion map algorithm<sup>21</sup> (tm-dmap) modifies the right normalization of the kernel to incorporate a user-provided target measure  $\mu(x)$ . The target measure does not need to be normalized and it can be given in the form of a vector  $\{\mu(x_i)\}_{i=1}^N$  defined on the dataset. The dataset itself has a sampling density  $\rho(x)$  (not necessarily known) which tm-dmap reweights to replace with  $\mu(x)$ . The generator approximated by tm-dmap corresponds to the overdamped Langevin dynamics with stationary distribution  $\mu(x)$ , and is independent of the sampling density. For use in metastable systems in molecular dynamics, one can generate data from an enhanced sampling procedure, run diffusion maps on the data, and reweight the results to a provided target measure such as a specified Gibbs density.

The first step of tm-dmap is to compute the kernel density estimate  $\rho_\varepsilon(x)$  using (21). The *right-normalized* kernel is defined for a pair of data points  $x, x'$  as

$$k_{\varepsilon, \mu}(x, x') = k_\varepsilon(x, x') \frac{\mu^{1/2}(x')}{\rho_\varepsilon(x')}. \quad (24)$$

We note that one can write the action of the right-

normalized kernel on density-weighted functions  $f(x)$  as

$$\begin{aligned} & \int_{\Omega} k_{\varepsilon,\mu}(x,x')f(x')\rho(x')dx' \\ &= \int_{\Omega} k_{\varepsilon}(x,x')f(x')\mu^{1/2}(x')\frac{\rho(x')}{\rho_{\varepsilon}(x')}dx'. \end{aligned} \quad (25)$$

Hence the right normalization reweights the integration from the sampling density to the square root of the target measure.

Next, we wish to *left-normalize* the kernel with

$$\rho_{\varepsilon,\mu}(x) := \int_{\Omega} k_{\varepsilon,\mu}(x,x')\rho(x')dx' \quad (26)$$

and define the Markov operator  $\mathcal{P}_{\varepsilon,\mu}$  on  $f$  as

$$\mathcal{P}_{\varepsilon,\mu}f(x) = \frac{\int_{\Omega} k_{\varepsilon,\mu}(x,y)f(y)\rho(y)dy}{\rho_{\varepsilon,\mu}(x)}. \quad (27)$$

Finally, we define the operator  $\mathcal{L}_{\varepsilon,\mu}$  as

$$\mathcal{L}_{\varepsilon,\mu}f = \frac{\mathcal{P}_{\varepsilon,\mu}f - f}{\varepsilon}. \quad (28)$$

The discrete analog  $P_{\varepsilon,\mu}$  of the Markov operator (27) is an irreducible and aperiodic Markov chain that is in detailed balance with a discrete stationary measure  $\pi$ . Using kernel expansions in  $\varepsilon$ , one can show that the discrete stationary measure  $\pi$  converges to the continuous reweighting measure  $\frac{\mu(x)}{\rho_{\varepsilon}(x)}$  as  $N \rightarrow \infty$  and  $\varepsilon \rightarrow 0$ .

### III. PROPOSED METHODOLOGY

#### A. Target Measure Mahalanobis Diffusion Map

An important limitation of the original diffusion map<sup>17</sup> with isotropic kernels and the target measure diffusion map<sup>15,21</sup> is that they only approximate generators that are relevant for gradient flows. These methods utilize the sampling density and user-input target measure, but not dynamical properties of the data. They are capable of approximating the committer only for the overdamped Langevin dynamics

$$dx = -\nabla F(x)dt + \sqrt{2\beta^{-1}}dw$$

and cannot account for anisotropic and position-dependent diffusion tensor  $M(x)$ . Consequently, to approximate generators for diffusion processes with position-dependent noise, the diffusion map algorithm requires modification.<sup>18,21</sup> Position-dependent diffusion is essential in dynamical models for collective variables, tracing back to Kramer's model for diffusive barrier crossing.<sup>49</sup> This diffusion naturally arises from the coupling of collective variables to the solvent<sup>31,50</sup> and heavily influences the reaction pathway and reaction coordinate in problems such as protein folding<sup>51</sup> and membrane permeation.<sup>52</sup>

In our recent work,<sup>16</sup> we proved that the Mahalanobis diffusion map algorithm (mmap) approximates the generator for

the overdamped Langevin dynamics in collective variables (7) with  $O(\varepsilon)$  accuracy and applied mmap to collective variable data of MD simulations of Lennard-Jones-7 in 2D and of the transition between metastable states C7eq and C5 of alanine dipeptide in vacuum. Importantly, we were not able to apply mmap to the transition C7eq-C7ax in alanine dipeptide because of the lack of data in the transition region sampled from the invariant density required for mmap.

The mmap algorithm uses the Mahalanobis kernel introduced by Singer and Coifman<sup>18</sup>

$$k_{\varepsilon}(x,x') = \exp\left\{\frac{-(x-x')^{\top}[M^{-1}(x)+M^{-1}(x')(x-x')]}{4\varepsilon}\right\} \quad (29)$$

where each  $M(x)$  is a user-input  $d \times d$  symmetric positive-definite matrix considered as the diffusion matrix for data point  $x$ . The difference between each component of  $x$  and  $x'$  is normalized by the corresponding variance and reflects the difficulty to deviate along each direction. Therefore, the Mahalanobis kernel (29) is a decaying exponential of Mahalanobis distance squared, and is designed to account for anisotropy of the diffusion process the data is coming from.

In this work, we have extended the results of Ref. 16 to target measure diffusion map resulting in the *target measure Mahalanobis diffusion map* algorithm abbreviated as tm-mmap. The key modification in tm-mmap in comparison with tm-dmap is that the right normalization of the kernel function (24) is changed to

$$k_{\varepsilon,\mu}(x,x') = k_{\varepsilon}(x,x')\frac{(\mu(x')|M(x')|^{-1/2})^{1/2}}{\rho_{\varepsilon}(x')}, \quad (30)$$

where  $|M(x')|$  denotes the determinant of  $M(x')$ . The tm-mmap algorithm is written out in the panel Algorithm 1.

---

#### Algorithm 1: Target Measure Mahalanobis Diffusion Map (tm-mmap)

---

**Input:** data  $X = \{x_i\}_{i=1}^N$ , diffusion matrices  $\{M(x_i)\}_{i=1}^N$ , bandwidth  $\varepsilon$ , target measure  $\mu$ ,

**Output:** Generator matrix  $L_{\varepsilon}$

Construct kernel from (29), estimate sampling density

1  $[K_{\varepsilon}]_{i,j} = k_{\varepsilon}(x_i,x_j), i, j = 1, \dots, N$

2  $c_i = (2\pi\varepsilon)^{d/2}|M_i|^{1/2}, i = 1, \dots, N$

3  $[p_{\varepsilon}]_i = \frac{1}{Nc_i} \sum_j [K_{\varepsilon}]_{i,j}, i = 1, \dots, N$

Right normalize the kernel

4  $[K_{\varepsilon,\mu}]_{ij} := \frac{[K_{\varepsilon}]_{ij}(\mu_j|M_j|^{-1/2})^{1/2}}{[p_{\varepsilon}]_j}, i, j = 1, \dots, N$

Left normalize the kernel

5  $[P_{\varepsilon,\mu}]_{ij} := \frac{[K_{\varepsilon,\mu}]_{ij}}{\sum_{\ell} [K_{\varepsilon,\mu}]_{i\ell}}, i, j = 1, \dots, N$

Construct generator

6  $[L_{\varepsilon,\mu}]_{ij} = \frac{[P_{\varepsilon,\mu}]_{ij} - \delta_{ij}}{\varepsilon}, i, j = 1, \dots, N$

---

Suppose that we have a sampling procedure that allows us to generate a dataset  $\{x_i\}_{i=1}^N$  of any size  $N$  distributed according to an arbitrary measure  $\mu'(x)$  such that the target measure

$\mu(x)$  is absolutely continuous with respect to  $\mu'$ . This means  $\mu'(A) = 0$  implies that  $\mu(A) = 0$  for any measurable set  $A$ . We claim that given

- a smooth target measure  $\mu(x)$  and
- a smooth symmetric positive definite diffusion matrix function  $M(x)$  whose inverse has entries growing not faster than a polynomial and determinant bounded away from zero,

the matrix operator  $L_{\varepsilon, \mu}$  constructed according to Algorithm 1 tends to the integral operator  $\mathcal{L}_{\mu, \varepsilon}$  from (28) as  $N \rightarrow \infty$  which, in turn, tends to the generator of the overdamped Langevin dynamics in collective variables (7) as  $\varepsilon \rightarrow 0$ . I.e., for every smooth function  $f(x)$  we have:

$$\begin{aligned} \lim_{\varepsilon \rightarrow 0} \lim_{N \rightarrow \infty} \sum_{j=1}^N [L_{\varepsilon, \mu}]_{ij} [f]_j &= \lim_{\varepsilon \rightarrow 0} [\mathcal{L}_{\varepsilon, \mu} f](x_i) \\ &= \frac{\beta}{2} [\mathcal{L} f](x_i) \end{aligned} \quad (31)$$

for all  $1 \leq i \leq N$ . The limit  $N \rightarrow \infty$  in (31) follows from the law of large numbers. The limit in  $\varepsilon \rightarrow 0$  requires a careful proof, which is provided in Appendix B.

## B. Transition Path Theory in Collective Variables with Diffusion Maps

To obtain the committor, we solve the matrix equation

$$\begin{aligned} [L_{\varepsilon, \mu} q]_i &= 0, & x_i \in \Omega \setminus (A \cup B), \\ [q]_i &= 0, & x_i \in A, \\ [q]_i &= 1, & x_i \in B. \end{aligned} \quad (32)$$

Since  $L_{\varepsilon, \mu}$  approximates the generator  $\mathcal{L}$  for the overdamped Langevin dynamics in collective variables, (7), the solution to (32) converges to the solution to the corresponding committor problem (10) where  $\mathcal{L}$  is given by (7). Once the committor is found, one can calculate the other quantities of interest: the probability density of reactive trajectories, the reactive current<sup>16</sup> on the data, and the transition rate.

To compute the reactive current, we need an estimate for the target density  $\pi(x) := Z^{-1} \mu(x)$ , with  $Z = \int_{\mathbb{R}^d} \mu(x) dx$ . If we don't have access to  $Z$ , we can estimate this with the kernel density estimate  $p_\varepsilon$  from (21). Then, we estimate  $Z$  via Monte Carlo integration with kernel reweighting as

$$Z_\varepsilon := \frac{1}{N} \sum_{i=1}^N \frac{\mu(x_i)}{[p_\varepsilon]_i}$$

as for sufficiently large  $N$  and small  $\varepsilon$  we have

$$Z_\varepsilon \approx \int_{\mathbb{R}^d} \frac{\mu(x)}{\rho(x)} \rho(x) dx = Z.$$

We estimate the discrete reactive current  $\hat{\mathcal{J}}_\varepsilon \in \mathbb{R}^{d \times N}$  using the formula

$$[\hat{\mathcal{J}}_\varepsilon]_{\alpha i} := \frac{\mu(x_i)}{\beta Z_\varepsilon} \sum_j [L_\varepsilon]_{ij} ([q_\varepsilon]_i - [q_\varepsilon]_j) (x_i^\alpha - x_j^\alpha), \quad (33)$$

where  $1 \leq \alpha \leq d, 1 \leq i \leq N$ .

The reaction rate  $\hat{\nu}_{AB}$  is estimated via a reweighted Dirichlet form of the committor  $[q]$ :

$$\hat{\nu}_{AB} = \frac{1}{|I_{AB}|} \sum_{i \in I_{AB}} [L_\varepsilon]_{ij} ([q_\varepsilon]_i - [q_\varepsilon]_j)^2 \frac{\mu(x_i)}{Z_\varepsilon [p_\varepsilon]_i} \quad (34)$$

where  $I_{AB} = \{i : x_i \in \Omega \setminus (A \cup B)\}$ . An in-depth description justifying formulas (33) and (34) is found in Appendix D in Ref. 16.

## C. Choosing $\varepsilon$

In practice, the limit  $\varepsilon \rightarrow 0$  cannot be taken for a finite dataset. Instead, one generally tries to choose  $\varepsilon$  as small as possible without causing instability in the corresponding kernel matrix. Intuitively one can think of choosing  $\varepsilon$  too small as isolating nodes in the graph (equivalently as creating a row of zeros in  $L_{\varepsilon, \mu}$ ), and too large as losing local structure in the graph. We note that many heuristics exist for choosing the scaling parameter  $\varepsilon$  in diffusion maps, relating back to bandwidth selection in kernel density estimation<sup>53</sup>. For this work we choose the method of Berry, Harlim and Giannakis<sup>25–28</sup> which we refer to as the ‘‘Ksum test’’.

The idea for the heuristic is to find the range of  $\varepsilon$  where the asymptotic results of diffusion maps hold true for the given dataset. We find this range by analyzing the double sum

$$S(\varepsilon) := \sum_{i=1}^N \sum_{j=1}^N [K_\varepsilon]_{ij}$$

over a range of  $\varepsilon$  values. Here,  $[K_\varepsilon]_{ij} = k_\varepsilon(x_i, x_j)$  where  $k_\varepsilon$  is the Mahalanobis kernel (29). For large enough  $\varepsilon$ ,  $[K_\varepsilon]_{ij} \approx 1$  for all  $i, j$ , and  $S(\varepsilon) \rightarrow N^2$ . Conversely, for small enough  $\varepsilon$ ,  $[K_\varepsilon]_{ij} \approx 0$  for all  $i, j$  with  $i \neq j$  and since  $[K_\varepsilon]_{ii} = 1$  we can say  $S(\varepsilon) \rightarrow N$  as  $\varepsilon \rightarrow 0$ . Using a series expansion of  $\log S(\varepsilon)$  one can show that

$$\log S(\varepsilon) \approx \frac{d}{2} \log \varepsilon + O(\varepsilon),$$

which is the range where the diffusion map convergence to the generator should hold. Thus, if we plot  $\log \varepsilon$  against  $\log S(\varepsilon)$ , we should see a linear region of slope approximately  $\frac{d}{2}$ , where  $d$  is the dimension of the dataset. On the other hand, as we have just discussed, the slope of this graph should tend to zero as  $\varepsilon \rightarrow 0$  and as  $\varepsilon \rightarrow \infty$ . Therefore, we expect to have  $\frac{\partial \log S(\varepsilon)}{\partial \log \varepsilon} \approx \frac{d}{2}$  where the slope is maximal. For practical calculation, it is useful to note that

$$\frac{\partial \log S(\varepsilon)}{\partial \log \varepsilon} = - \frac{\sum_{i,j=1}^N [K_\varepsilon]_{ij} \log [K_\varepsilon]_{ij}}{\sum_{i,j=1}^N [K_\varepsilon]_{ij}}. \quad (35)$$

The procedure for choosing a good bandwidth  $\varepsilon^*$  is outlined in Algorithm 2 in Appendix A.

#### D. Diffusion Map Implementation

The approximation error for diffusion maps scales as  $O(N^{-1/2})$  where  $N$  is the number of data points. On the other hand, the kernel matrix is dense as the exponential function in the kernel function is always positive, though exponentially decaying. Therefore, it is important to utilize a sparse approximation for the kernel matrix  $\tilde{K}_\varepsilon$ . Typically practitioners will use a  $k$ -nearest neighbors (KNN) approach or a radius-nearest neighbors (RNN) approach. We prefer the RNN-based sparse approximation as it gives results consistent with our expectations even if the choice of the bandwidth is poor and it does not require symmetrization of  $\tilde{K}_\varepsilon$ . The radius nearest neighbors approach uses

$$\tilde{k}_\varepsilon(x, x') = \begin{cases} k_\varepsilon(x, x'), & d(x, x') \leq r \\ 0, & \text{otherwise} \end{cases}, \quad (36)$$

where  $d(x, x')$  is the distance used in the kernel and  $r$  is typically chosen to be  $3\sqrt{\varepsilon}$ .

To implement  $\text{tm-mmap}$  where data points  $x, x'$  are on a Torus (such as for dihedral angles), we compute the Mahalanobis kernel (29) with periodic reflections in computing the distance vector  $x - x'$ .

#### E. Metadynamics

For enhanced sampling we utilize the well-tempered metadynamics algorithm (WTMETAD).<sup>54</sup> WTMETAD is an adaptive enhanced sampling algorithm which updates the potential of the simulation as the trajectory progresses. At the  $n$ th biasing step, the existing bias at the current location  $x_n$  is contributed to the bias term

$$V_n(x) = V_{n-1}(x) + \left[ h e^{-(x-x_n)^\top \Sigma^{-1} (x-x_n)} \right] \left[ e^{-\frac{\beta}{\gamma-1} V_{n-1}(x_n)} \right] \quad (37)$$

for the  $n$ th biasing step. The bias function parameters are the height of the biasing kernel  $h$ , the covariance matrix  $\Sigma$ , and the biasing factor  $\gamma$ . Usually, the covariance is chosen to be a diagonal matrix  $\Sigma = \text{diag}(\sigma_1, \dots, \sigma_d)$  where  $\sigma_j$ ,  $1 \leq j \leq d$  are based on the unbiased CV fluctuations. The *well-tempered* variant of metadynamics is distinguished by the factor  $\exp\left(-\frac{\beta}{\gamma-1} V_{n-1}(x_n)\right)$  which scales the Gaussian biases. In the limit  $\gamma \rightarrow 1$ , the well-tempered term tends to 0 and there is no biasing, while for  $\gamma \rightarrow \infty$  we have the well-tempered term tending to 1 and recover the usual metadynamics algorithm. The user also chooses a timestep  $t_{\text{bias}} = n_{\text{bias}} \Delta t$ , where  $\Delta t$  is the timestep of the simulation. As the simulation runs, the height of the deposited Gaussian bumps decreases. As a result, the total biasing potential becomes less rugged as the metadynamics run progresses. Moreover, it converges to  $-(1 - \frac{1}{\gamma})F(x)$ , particularly the negative of the free energy as  $\gamma \rightarrow \infty$ . Hence, in the long run, metadynamics flattens out the free energy and with large  $\gamma$  will fill its level sets uniformly with samples. We utilize well-tempered metadynamics because of its convergence guarantees<sup>55,56</sup> and its improved reweighting over the standard metadynamics.<sup>57</sup>

#### F. Obtaining free energy and diffusion matrix in high dimensions

Besides the dataset,  $\text{tm-mmap}$  requires the target measure and the diffusion matrix evaluated at the data points. The evaluation of the diffusion matrix is computationally demanding but straightforward using local restrained simulations.<sup>6</sup> The evaluation of the target measure if it is not known a priori is less straightforward. We propose a method for estimating the target measure  $\mu = \exp(-\beta F(x))$  in high dimensions that works with any enhanced standard sampling algorithm with known biasing potential. This method is inspired by Ref. 57.

Suppose that an enhanced sampling algorithm samples from the Gibbs density

$$\rho(x) \propto e^{-\beta(F(x)+U(x))},$$

where  $U$  is a *known* bias potential, while  $F(x)$  is the *unknown* free energy. The desired target measure is  $\mu(x) = \exp(-\beta F(x))$ . We approximate the sampling density  $\rho(x)$  by  $\rho_\varepsilon(x)$  given by (21) and obtain the following estimate for the target measure:

$$\mu(x) \approx \rho_\varepsilon(x) \exp(\beta U(x)). \quad (38)$$

#### G. Preparing the dataset

A remarkable property of  $\text{tm-mmap}$  is that it allows for the use of input data distributed according to an arbitrary measure  $\mu'$  provided the target measure  $\mu$  is absolutely continuous with respect to  $\mu'$ . In practice, this means that the data points should cover all regions where the target measure  $\mu$  is above a certain threshold that should be strictly smaller than the value of the target measure at the transition state. Therefore,  $\text{tm-mmap}$  enables us not only to generate data points using any enhanced sampling algorithm but also post-process them as we desire. In this work, we used two enhanced sampling algorithms to generate data: temperature acceleration and well-tempered metadynamics (see Section III.E). We generated long trajectories using these enhanced sampling algorithms and then post-processed them to leave roughly  $N = 10^4$  points as follows:

- Trajectory data generated using temperature acceleration were subsampled uniformly in time.
- Trajectory data generated by well-tempered metadynamics were subsampled
  - uniform in time;
  - quasi-uniform in space resulting in the so-called *delta-net*.<sup>58</sup>

We compare the performance of  $\text{tm-mmap}$  on these three types of datasets and show that the the *delta-net* data lead to the most accurate and the most robust results. The construction of the *delta-net* is detailed in Algorithm 3 in Appendix A.

#### IV. NUMERICAL TESTS

In this section we test `tm-mmap` on two examples: the Moro-Cardin two-well system with position-dependent diffusion, and on alanine dipeptide with two dihedral angles in vacuum. The results of `tm-mmap` are compared to those computed by means of the finite element method (FEM). We weigh the numerical error according to the probability density of reactive trajectories:

$$E = \sum_{i=1}^N |q(x_i) - q_{FEM}(x_i)| w(x_i), \quad (39)$$

$$w(x_i) = \frac{\mu(x_i)q(x_i)(1 - q(x_i))}{\sum_j \mu(x_j)q(x_j)(1 - q(x_j))}. \quad (40)$$

The resulting error will be abbreviated as WAE (Weighted Absolute Error).

In addition, we apply `tm-mmap` to alanine dipeptide with four dihedral angles where finite element method becomes infeasible.

##### A. The Moro-Cardin System

The Moro-Cardin two-well system with position-dependent diffusion<sup>24</sup> is a simple and insightful example featuring saddle avoidance. The system evolves according to SDE (3) with the potential function  $F(x) \equiv V(x)$  and diffusion matrix  $M(x)$  are given by

$$V(x) = 5(x_1^2 - 1)^2 + 10\alpha x_2^2, \quad (41)$$

$$M(x) = (1 + 8e^{-\|x\|^2/2\sigma^2})^{-1} I_{2 \times 2}, \quad (42)$$

where  $\sigma = 0.2$  and  $\alpha = \arctan(7\pi/9)$ . The inverse temperature-like parameter  $\beta$  in SDE (3) is chosen to be 1. The diffusion matrix  $M(x)$  is close to the identity matrix everywhere except for a ball around the origin of radius  $2\sigma = 0.4$ , while it decays to  $(1/9)I_{2 \times 2}$  at the origin. The function  $V(x)$  has two minima at  $(-1, 0)$  and  $(1, 0)$ , and a saddle at the origin. The sets  $A$  and  $B$  are chosen to be balls centered at the minima of radius 0.2. Level sets of the potential function and the diffusion coefficient are depicted in Figure 2.

The dynamics of the Moro-Cardin system feature *saddle avoidance* (see Figure 3). Those reactive trajectories that pass near the saddle are slowed down by low diffusivity so much that they get stuck in this region for a long time. As a result, the reactive trajectories that climb over higher barriers and avoid the low-diffusivity region surrounding the origin will surpass the those that go over a lower barrier but get trapped in the low-diffusivity region. As a result, the reactive flux splits into two reaction channels bending around the origin from above and from below.

We created three datasets as described in Section III.G. The first dataset, denoted by `hightemp`, was generated by running a long trajectory using the Euler-Maruyama method with time step  $dt = 10^{-4}$  for  $10^6$  steps at a high temperature  $\beta^{-1} = 3$ ,

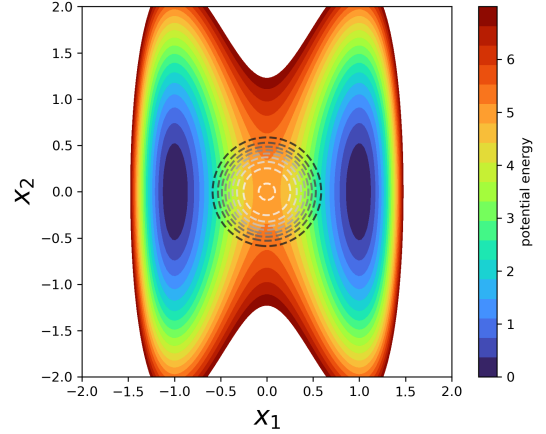


**FIG. 2:** The potential energy function (color coding) and the level sets of the diffusion coefficient (dashed circles of grey shades) for the Moro-Cardin system. The level sets of the diffusion coefficient indicate a low-diffusivity region around the origin.

and then subsampling the trajectory at equispaced time intervals. The second and third datasets were generated using WT-METAD with parameters  $h = 0.35$ ,  $\sigma_1 = \sigma_2 = 0.1$ ,  $\gamma = 5.0$  and deposition rate of every 500 timesteps (see Section III.E). Then the datasets `metad` and `deltanet` were obtained, respectively, by subsampling WT-METAD trajectory data uniformly in time and quasi-uniformly in space using Algorithm 3 with  $\delta = 0.017$ . All datasets contain a total of  $N = 10^4$  data points.

For each of these datasets, we computed the matrix operator  $L_{\varepsilon, \mu}$  using Algorithm 1 and then computed the committor, the reactive current, and the transition rate as described in Section III.B.

For validation, we also computed the committor, the reactive current displayed in Figure 3, and the transition rate using the finite element method (FEM). The points of the finite element mesh were used as the test points  $x_i$ . The error metric for the committor was the weighted absolute error (WAE) defined in (39)–(40).

The committors and the reactive currents for the `hightemp`, `metad` and `deltanet` datasets are shown in Figure 4. The errors in the committor and the transition rate measured against the FEM solutions for all three datasets are plotted in Fig. 5. The dashed vertical lines correspond to the values of the bandwidth parameter  $\varepsilon$  obtained using Algorithm 2. The error plots indicate that the `deltanet` dataset leads to the most accurate results and most robust with respect to the choice of the bandwidth parameter  $\varepsilon$ . In particular, the discrepancy between the transition rate computed by `tm-mmap` for the `deltanet` dataset and the FEM rate is within 5% for a broad range of epsilon values:  $2 \cdot 10^{-3} < \varepsilon < 10^{-1}$ . The results obtained for the `hightemp` dataset are the least accurate and least robust.

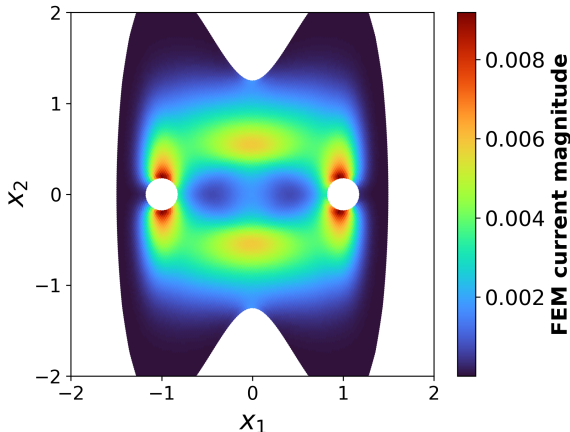


**FIG. 3:** The reactive current computed for the Moro-Cardin system (Section IV.A) using the finite element method.

### B. Alanine dipeptide with two dihedral angles

Alanine dipeptide (Figure 6) is a small biomolecule commonly used for benchmarking rare event algorithms for MD simulation. Its free energy in two dihedral angles  $\phi$  and  $\psi$  has three local minima (Figure 7) making it a popular test example in chemical physics.<sup>5,6,15,59</sup> The close minima C5 and C7eq are separated from each other by a low free energy barrier of about 5 kJ/mol. The remote minimum C7ax is separated from C7eq by a barrier of approximately 40 kJ/mol. The transition between C5 and C7eq was quantified using `mmap`<sup>16</sup> because adequate data for this purpose could be collected by sampling from the invariant density. Now we are interested in the transition between the C7ax and C7eq metastable states. Powerful enhanced sampling such as WTMETAD is required for obtaining an adequate data coverage for this transition.

A typical set of collective variables effectively representing its motion consists of two to four of its dihedral angles.<sup>6,55,59,60</sup> In contrast to previous uses of diffusion maps on alanine dipeptide<sup>8,15,41</sup> we utilize the dihedral angles as input coordinates for diffusion maps. For numerical tests, we choose the set of only two dihedral angles  $\phi$  and  $\psi$ , as the finite element method can be used for validation in this case. The space  $\Omega$  of the collective variables  $(\phi, \psi)$  is the square  $[-\pi, \pi]^2$  glued into the torus  $\mathbb{T}^2$ .

In order to generate datasets for alanine dipeptide, we ran a long metadynamics trajectory using GROMACS<sup>61</sup> and WT-METAD. A velocity-rescaling thermostat was used to set the temperature to 300K in a vacuum under constant number, volume, and temperature (NVT) conditions. The timestep was set to 2 femtoseconds, while the total simulated time interval was 10 nanoseconds. The parameters for WTMETAD were  $h = 1.2$ ,  $\sigma = 0.2$ , and  $\gamma = 6$ . Then the dataset denoted by `metad` was obtained by subsampling the trajectory data uniformly in time to make a total of  $N = 10^4$  points. The second dataset `deltanet` obtained from the trajectory data by Algorithm 3 with  $\delta = 0.04$  also contains  $N = 10^4$  points.

The diffusion matrices  $M(x_i)$ ,  $1 \leq i \leq N$ , are visualized in

Figure 8. We utilized the software PLUMED<sup>59</sup> to obtain the derivatives of the dihedral angles with respect to the atomic coordinates and to obtain the restrained averages. The reactant and product sets  $A$  and  $B$  are the circles of radius 0.349 centered at the C7eq and C7ax minima located at  $(-1.419, 1.056)$  and  $(4.358, 1.874)$  respectively.

The free energy  $F$  in  $x = (\phi, \psi)$  shown in Figure 7 was obtained from a separate WTMETAD simulation with biasing on  $\phi$  and  $\psi$ . The target measure is  $\mu(x) = e^{-\beta F(x)}$ .

The committor and the reactive current obtained using `tm-mmap` on the datasets `metad` and `deltanet` are compared to those computed by the finite element method (FEM) in Figures 9 and 10. For both datasets, the committor and the current by `tm-mmap` are similar to those by the FEM, but the results for `deltanet` are considerably less noisy. Moreover, the weighted absolute error (39)–(40) for the committor for `deltanet` is smaller than that for `metad` for most choices of  $\epsilon$ , in particular, it is smaller for the values of  $\epsilon$  suggested by Algorithm 2. The transition rate approximated by `tm-mmap` for the `deltanet` dataset differs by less than 10% from the rate obtained by FEM for a broad range of epsilon values. In particular, the  $\epsilon$ -value suggested by Algorithm 2 is very close to optimal. The FEM transition rate is  $6.6 \cdot 10^{-6} \text{ ps}^{-1}$ , while the `tm-mmap` with `deltanet` transition rate at  $\epsilon$  suggested by Algorithm 2 is  $6.3 \cdot 10^{-6} \text{ ps}^{-1}$ .

## V. APPLICATION: ALANINE DIPEPTIDE WITH FOUR DIHEDRAL ANGLES

While only two dihedral angles are needed for enhanced sampling of the configurational space of alanine dipeptide<sup>57</sup>, at least three dihedral angles are required to adequately describe the transition mechanism from C7eq to C7ax.<sup>6,29,62–64</sup> The `tm-mmap` algorithm is a suitable tool for computing the committor in 4D. Therefore, we consider the dynamics of alanine dipeptide represented by four dihedral angles  $(\phi, \psi, \theta, \zeta)$ . The collective variable space is the four-dimensional torus  $\mathbb{T}^4$  obtained by an appropriate gluing of the four-dimensional hypercube  $[-\pi, \pi]^4$ .

### A. Simulation details

To generate the data, we first run WTMETAD to build a bias potential on a grid in the  $\phi$ - $\psi$  variables, with the same parameters as in Section IV.B. We then run a trajectory with the fixed bias to obtain  $N = 10^4$  data points  $x_i \in \mathbb{T}^4$ . Utilizing the kernel density estimate  $\rho_\epsilon(x)$  from (21) and the stored metadynamics bias  $U(x)$  we obtained an estimate to the target measure using equation (38).

We computed the  $4 \times 4$  diffusion matrices  $M(x_i)$  with the aid of the package PLUMED from equation (5) as described in Ref. 6. The  $2 \times 2$  sub-matrices corresponding to each possible pair of dihedral angles are visualized in Figure 11. The sub-matrices still correspond to a conditional average on  $(\phi, \psi, \theta, \zeta)$  rather than a particular pair of dihedrals. Despite this, the  $\phi$ - $\psi$  sub-matrices are virtually indistinguishable from



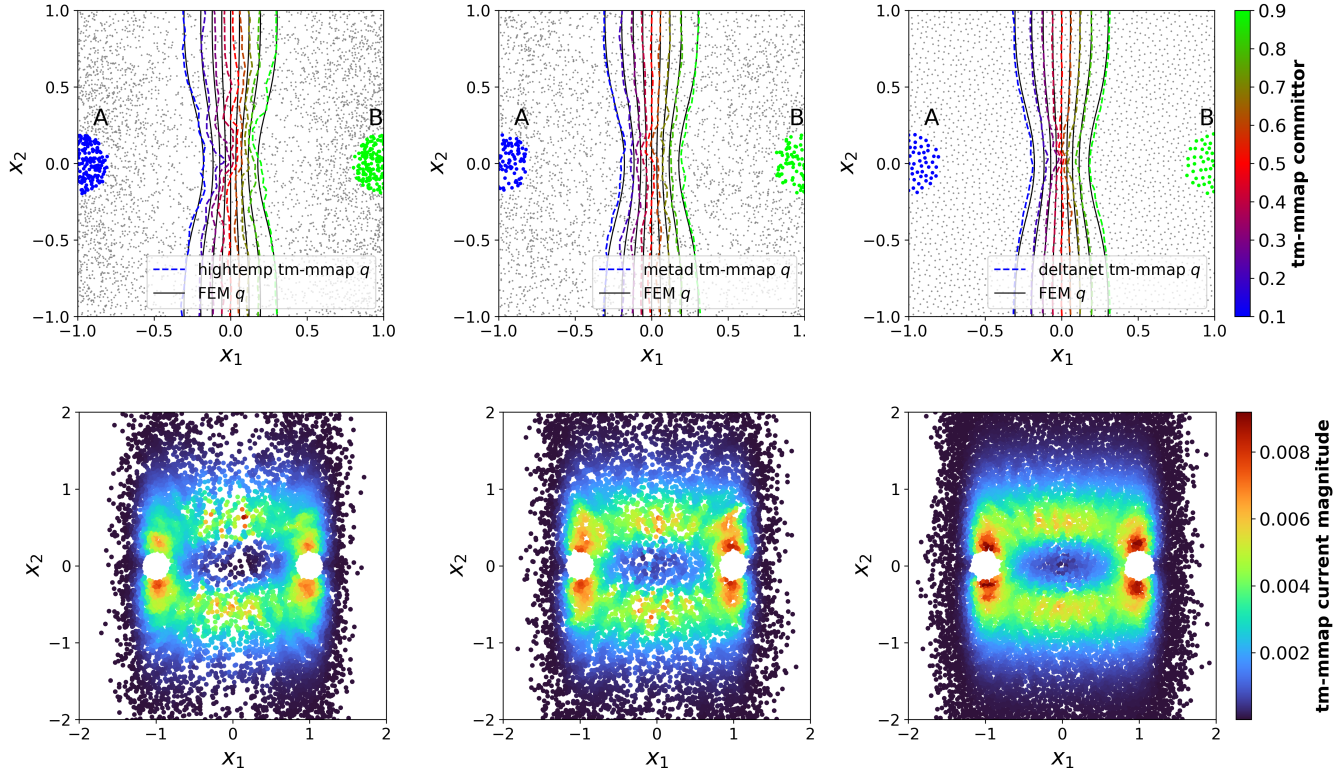


**FIG. 4:** An application of  $\text{tm-mmap}$  to the Moro-Cardin system (Section IV.A). Committor level sets (top row) and reactive current magnitudes (bottom row) computed by  $\text{tm-mmap}$  using three datasets as input. Left column: dataset *hightemp*: temperature accelerated molecular dynamics data for  $\beta^{-1} = 3$  subsampled uniformly in time. Middle column: dataset *metad*: WTMETAD trajectory data subsampled uniformly in time. Right column: dataset *deltanel*: WTMETAD trajectory data subsampled quasi-uniformly in space using Algorithm 3. The levelsets of the committor computed using  $\text{tm-mmap}$  (dashed colored curves) are superimposed with the level sets of the committor computed using the finite element method (solid black curves).

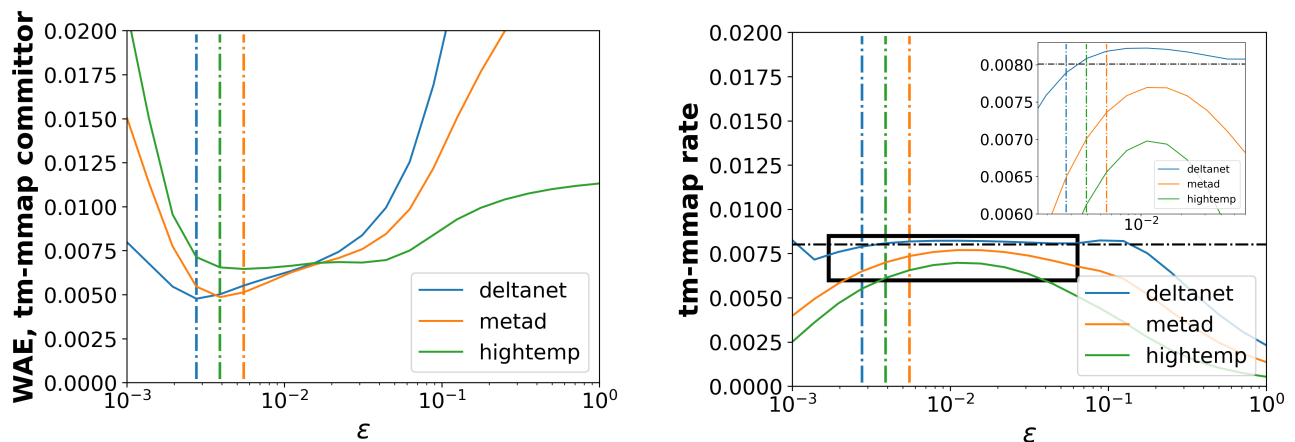


**FIG. 5:** An application of the  $\text{tm-mmap}$  to the Moro-Cardin system (Section IV.A). Left: Weighted absolute error (39)–(40) for the committor computed by  $\text{tm-mmap}$  using the *hightemp*, *metad*, and *deltanel* datasets. The committor computed using the finite element method is taken as the ground truth. The dotted lines indicate the epsilon chosen from the Ksum test (Algorithm 2). Right: A comparison of the transition rates computed from the  $\text{tm-mmap}$  committors (colored curves) for a range of values of the bandwidth coefficient  $\epsilon$  to the transition rate obtained via using the finite element method (dashed black line).



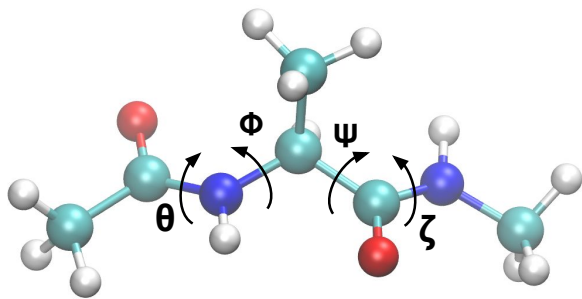


**FIG. 6:** Alanine dipeptide molecule with dihedral angles labelled.

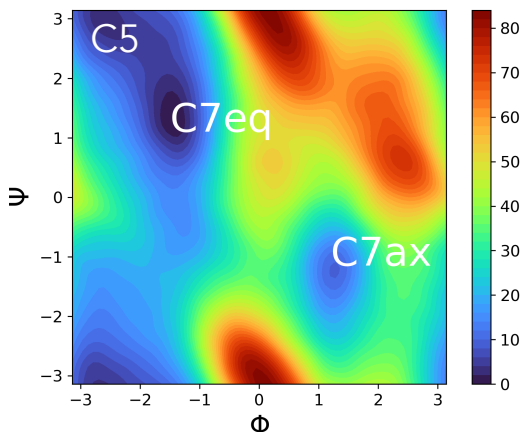


**FIG. 7:** Free energy landscape (kJ/mol) for alanine dipeptide in vacuum.

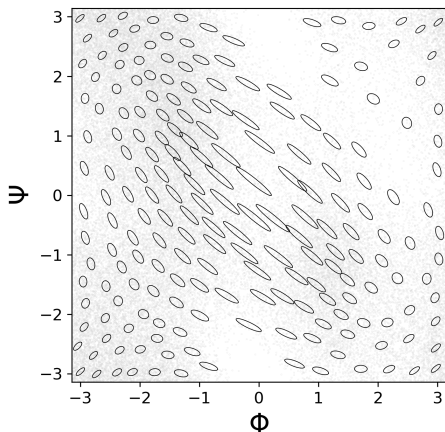


**FIG. 8:** A depiction of the diffusion matrix for alanine dipeptide in two dihedral angles. The ellipses correspond to the principal components of the estimated diffusion matrices evaluated at a representative subset of metadynamics data (faint grey dots).

those in Figure 8 for alanine dipeptide in only two dihedrals. This similarity to the un-averaged diffusion matrices in  $\phi, \psi$  was also noted in Ref. 65. We also point out the consistency of the  $\phi$ - $\theta$  and  $\psi$ - $\zeta$  plots in Figure 11 with the results obtained in Refs. 63 and 34, respectively. These similarities indicate that the partial derivatives of each dihedral angle with respect to the atomic coordinates are approximately constant on any fiber corresponding to a fixed value of this angle.

The reactant and product sets  $A$  and  $B$  in  $(\phi, \psi, \theta, \zeta)$ -coordinates were balls of radius 0.3 centered at  $(-1.443, 1.282, 0.027, -0.075)$  and  $(1.230, -1.206, -0.013, 0.099)$  respectively.

## B. Results

The results, the committor and the reactive current computed using `tm-mmap`, are displayed in Figure 12. In order to visualize functions of four variables in 2D we used projection and smoothing. For example, the committor  $\bar{q}(\phi, \psi)$  shown in Figure 12 (top left) is defined by:

$$\bar{q}(\phi, \psi) = \frac{1}{|S|} \sum_{x' \in S} q(x'), \quad \text{where} \quad (43)$$

$$S = \{x' = (\phi', \psi', \theta', \zeta') \in \mathbb{T}^4 \mid \sqrt{(\phi - \phi')^2 + (\psi - \psi')^2} < r\}.$$

The radius  $r$  was chosen to be 0.2 by trial and error. The committor  $\bar{q}(\phi, \theta)$  and the reactive currents displayed in Figure 12 were defined in a similar manner. Note that the reactive current in  $(\phi, \theta)$  is comparable in magnitude to the reactive current in  $(\phi, \psi)$ .

The transition rate for alanine dipeptide in four dihedral angles computed using (34) is  $2.0 \cdot 10^{-6} \text{ ps}^{-1}$ . This rate is comparable with the one obtained in Ref. 29 as a direct estimate from an unbiased very long trajectory trajectory simulated for 2.5 microseconds:  $1.4 \cdot 10^{-6} \text{ ps}^{-1}$ .

## VI. DISCUSSION

Our results indicate that the methodology developed in this work is a robust and powerful tool for quantifying rare events in systems described in terms of collective variables and governed by SDE (3). The dimensionality of the space of collective variables can be notably higher than what is feasible by traditional PDE solvers such as finite difference and finite element methods. The `tm-mmap` algorithm for computing the committor proposed in this work requires three pieces of input: a set of data points, the diffusion matrix and the target measure evaluated at the data points. Both the target measure and the diffusion matrix can be straightforwardly computed using standard software. The fact that the data points can be sampled from an arbitrary density with respect to which the target measure is absolutely continuous makes `tm-mmap` highly practical as any standard enhanced sampling software can be used for generating the input dataset.

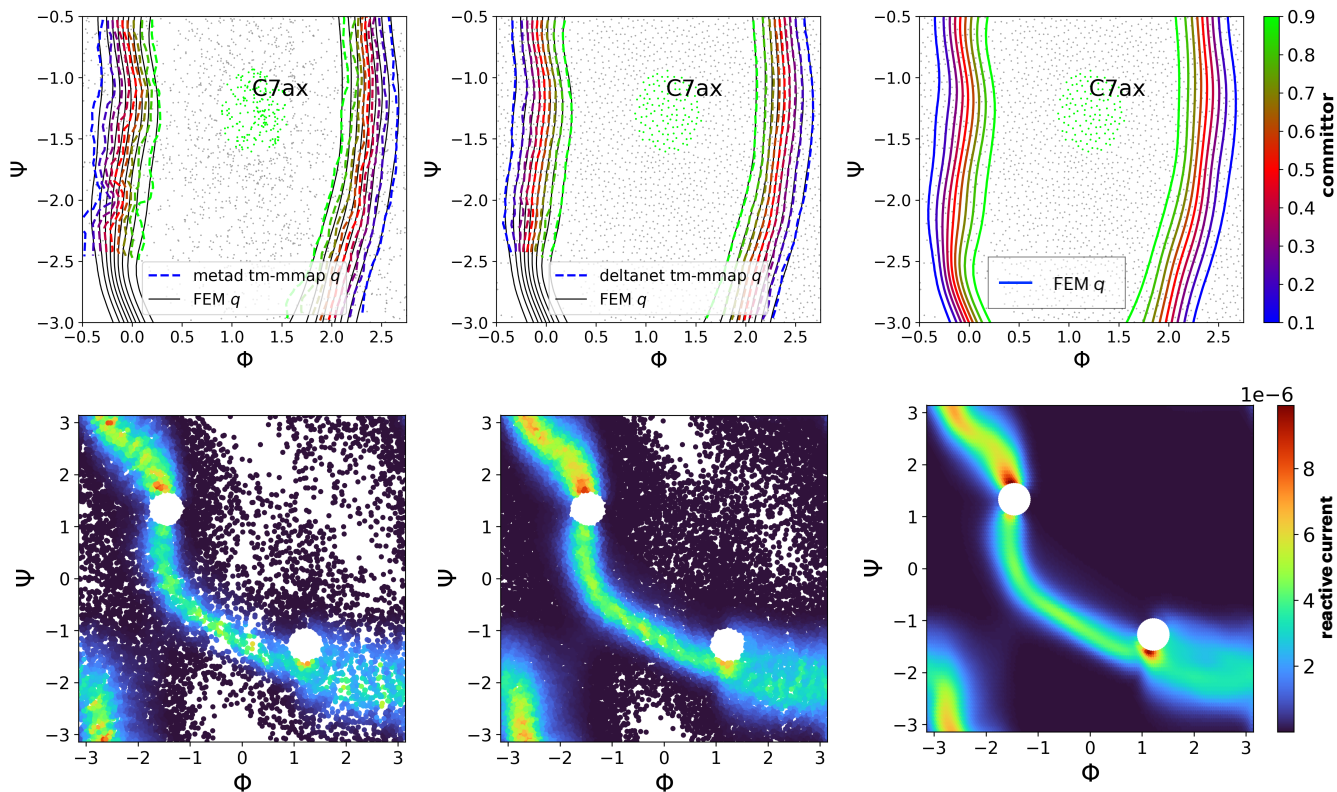


**FIG. 9:** The level sets of the committor and magnitude of the reactive current computed for alanine dipeptide in vacuum in  $(\phi, \psi)$  coordinates using tm-mmap for datasets meta-d (left column) and deltanet (middle column) and using finite element method (right column).

The computation of the diffusion matrices at the data points is the costliest part of the required input. For example, on a standard laptop a run of the tm-mmap algorithm for alanine dipeptide using a dataset of size  $N = 10^4$  takes from 5 to 30 seconds (depending on sparsity) whereas the computation of the diffusion matrices for it in four dihedral angles takes about 4 hours. In general other approaches such as the Kramer’s-Moyal expansion<sup>18,21,66</sup> and related “swarms of trajectories” approaches<sup>67,68</sup> can be used, and computational cost can be reduced by computing diffusion matrices on a subset of the data.<sup>69</sup>

We would like to point out that since the density for the input dataset is arbitrary, the user can generate a large initial dataset and then prune it in any manner. Our results for the Moro-Cardin system and for alanine dipeptide in two dihedral angles suggest that spatially quasi-uniform datasets obtained by constructing delta-nets (Algorithm 3) lead to the best results. It is very important that the committor and the transition rate remain close to the FEM rate treated as the ground truth for a broad range on values of  $\epsilon$ .

This observation suggests an investigation into how the numerical error in the committor committed by tm-mmap depends on the density of the input dataset. Is the uniformly distributed input dataset optimal? We leave this investigation for future work.

An important feature of the proposed methodology is that it yields numerical values for reactive current and the transition rate. Comparing the transition rate for alanine dipeptide represented in  $(\phi, \psi)$  ( $v_{AB} = 6.3 \cdot 10^{-6} \text{ ps}^{-1}$ ) and in  $(\phi, \psi, \theta, \zeta)$  ( $v_{AB} = 2.0 \cdot 10^{-6} \text{ ps}^{-1}$ ) we observe that the former is a factor of  $\sim 3.2$  larger than the latter. On the other hand, the rate for the four dihedral angles is in the ballpark of the estimate obtained from an unbiased very long trajectory.<sup>29</sup> This suggests the deficiency of two-dimensional representation of alanine dipeptide and emphasizes the importance of the ability of tm-mmap to work in higher dimensions.

## VII. CONCLUSION

We proposed a methodology for quantifying transition processes in molecular or biomolecular systems described in collective variables using the framework of the transition path theory and featuring the committor solver tm-mmap (Algorithm 1) based on diffusion maps and suitable for high dimensions (at least 4D as markedly shown in this work). The Mahalanobis kernel is capable of capturing the effects of variable and anisotropic diffusion ubiquitously arising in the dynamics in collective variables. The “target measure” variant of diffusion maps, on one hand, allows for input datasets being

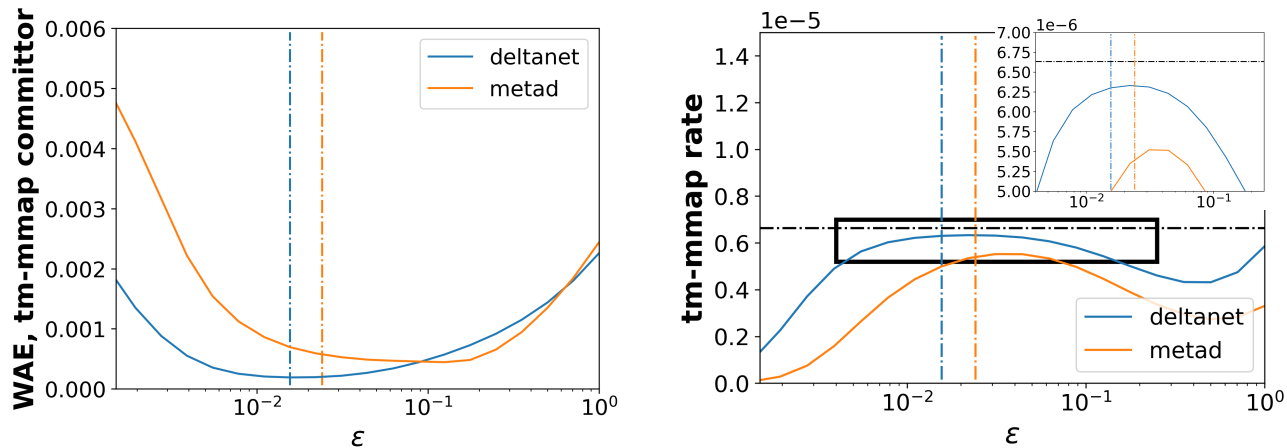


**FIG. 10:** Left: Weighted absolute errors (39)–(40) of the committor computed by  $\text{tm-mmap}$  for the alanine dipeptide in vacuum in  $(\phi, \psi)$  dihedral angles with respect to the committor computed by the finite element method. The dotted lines indicate the epsilon chosen by Algorithm 2. Right: Comparison of rates for  $\text{tm-mmap}$  on a range of  $\epsilon$  values, with zoom to area of the closest rate approximation. The dotted black line indicates the rate obtained by the finite element method.

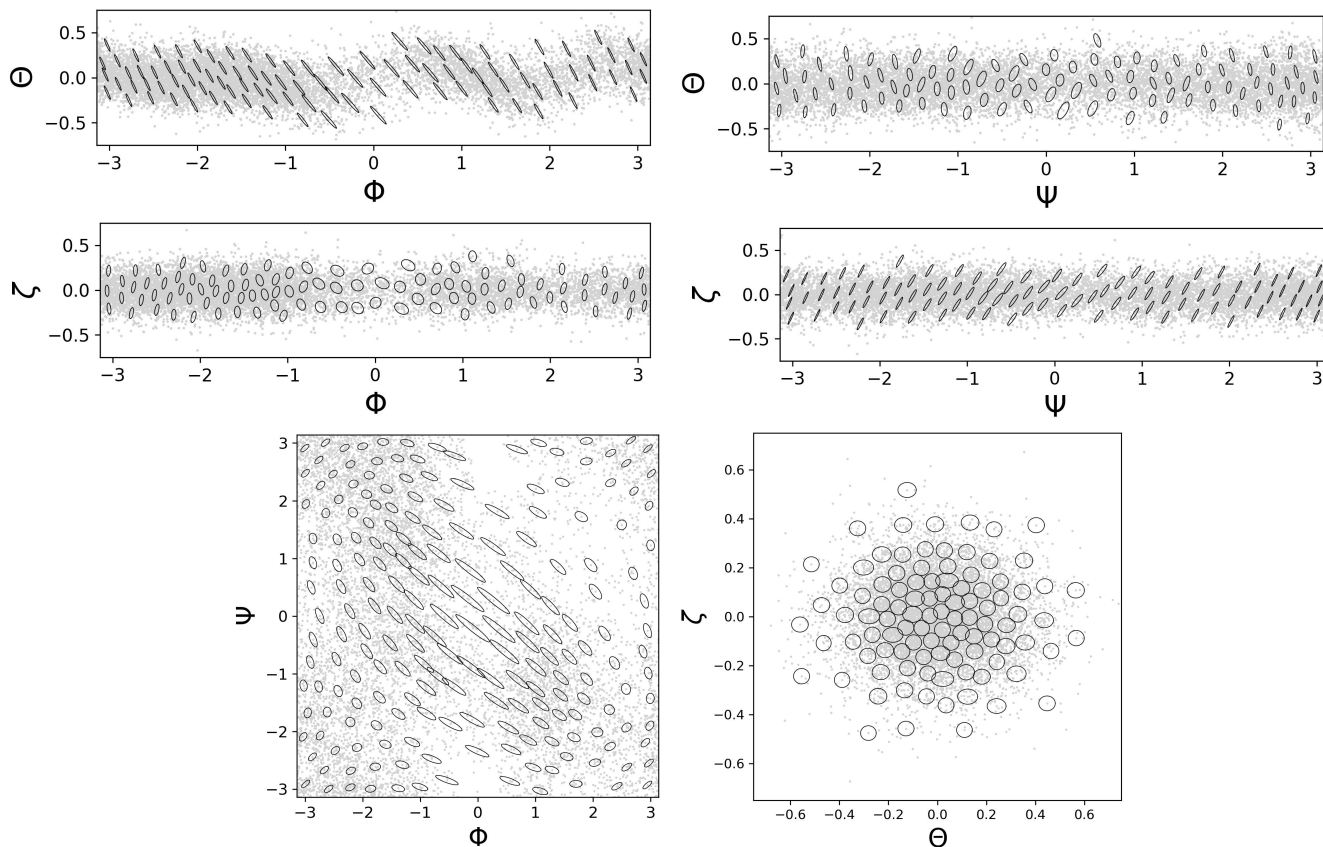


**FIG. 11:** Approximations of the principal components for the  $4 \times 4$  diffusion tensors obtained in all dihedrals for alanine dipeptide in vacuum. Each plot corresponds to principal components of the  $2 \times 2$  submatrices associated to each pair of dihedral angles.



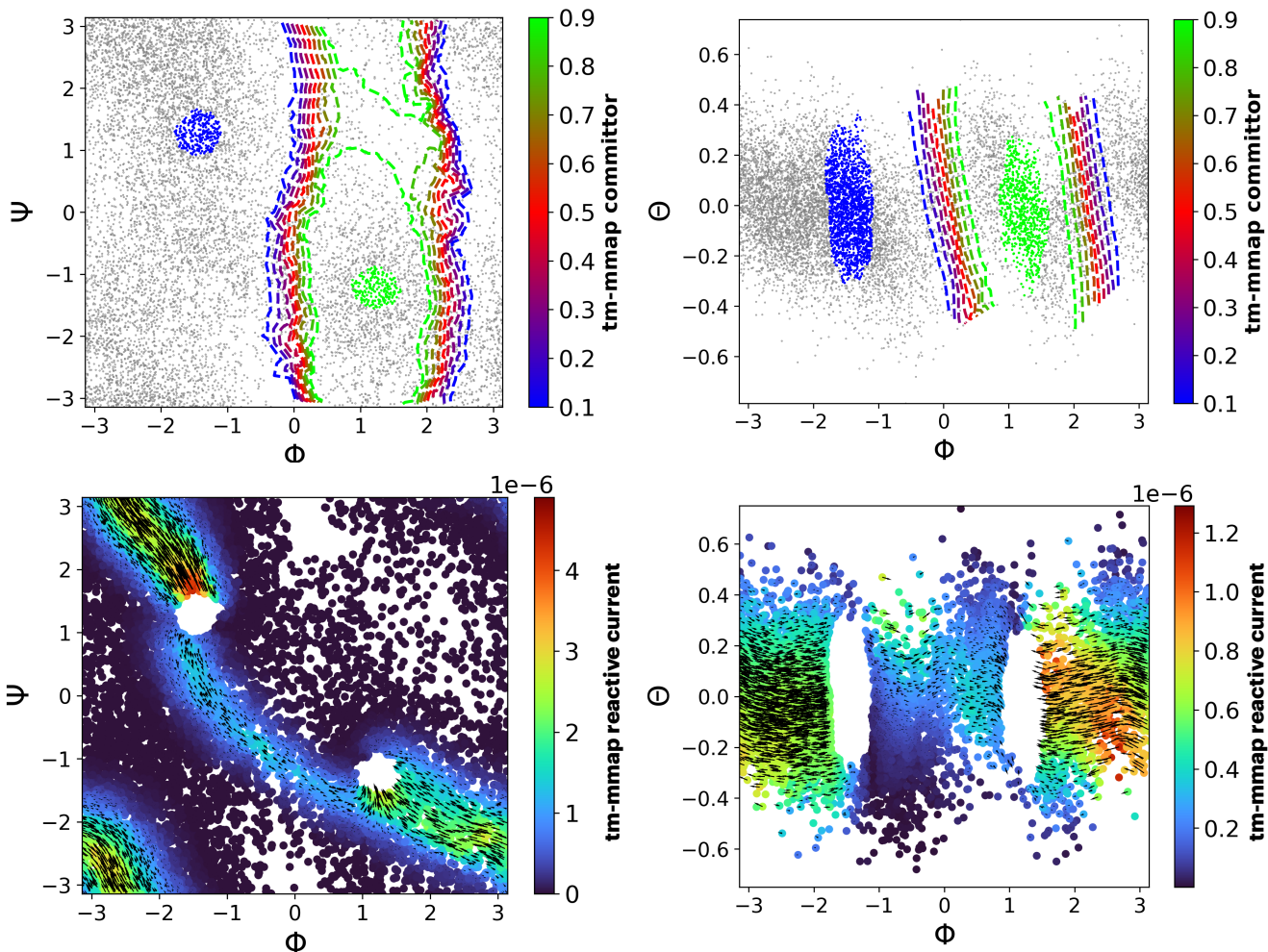


**FIG. 12:** The committor (top row) and the reactive current (bottom row) for alanine dipeptide in four dihedral angles computed using  $\text{tm-mmap}$ . The smoothed projection onto the  $(\phi, \psi)$ -space (left column) and the  $(\phi, \theta)$ -space (right column) was computed using equation (43).

sampled from an arbitrary density, while on the other hand, requires the input of the target measure that is usually unknown a priori. This challenge has been overcome by proposing a simple technique described in Section III.F that organically works with enhanced sampling and  $\text{tm-mmap}$ . The summary of our technical contributions is the following.

- An adjustment of the target measure diffusion map algorithm<sup>21</sup> for the use with the Mahalanobis kernel (29) resulting in the  $\text{tm-mmap}$  algorithm (Algorithm 1). The key step is the right normalization of the kernel function (30).
- A convergence proof of the discrete matrix operator built by  $\text{tm-mmap}$  to the generator for the overdamped Langevin dynamics in collective variables (7) given in Appendix B.
- A technique for estimating the unknown target measure in collective variable space that works with  $\text{tm-mmap}$

and any enhanced sampling algorithm with a stored biasing potential. The key formula is (38).

- The postprocessing of the enhanced sampling data resulting in a spatially quasi-uniform delta-net (Algorithm 3).

The numerical tests conducted on the Moro-Cardin system and on alanine dipeptide with two dihedral angles demonstrated the accuracy of  $\text{tm-mmap}$  for the committor, the reactive current, and the transition rate compared against the benchmark data produced by the finite element method. With regard to practical implementation, the tests against the benchmark illustrated the robustness of  $\text{tm-mmap}$  to the choice of the bandwidth parameter  $\varepsilon$  and close to optimal heuristic estimates for  $\varepsilon$  by the “Ksum test” (Algorithm 2)<sup>25–28</sup>. The spatially quasi-uniform datasets lead to the most accurate and the most robust results.

The application of  $\text{tm-mmap}$  to alanine dipeptide in four

dihedral angles gave a transition rate estimate from C7eq to C7ax that is reasonably close to the one extracted from an extremely long trajectory.<sup>29</sup>

We conclude that `tm-mmap` is a promising tool for rare-event quantification. It is accurate, robust, suitable for high dimensions, and easy-to-use.

## ACKNOWLEDGMENTS

This work was partially supported by AFOSR MURI grant FA9550-20-1-0397 (MC) and NSF CAREER grant CHE-2044165 (PT). Computing resources Deepthought2, MARCC and XSEDE (project TG-CHE180053) were used to generate molecular simulation data. We thank Dr. Bodhi Vani for valuable discussion on MD simulations of alanine dipeptide and Zachary Smith for advice on reweighting with WTMETAD.

## DATA AVAILABILITY STATEMENT

Implementation of the diffusion map code was inspired by the approach in the `pydiffmap` library.<sup>70</sup> The code for `tm-mmap` will be made available at <https://github.com/aevans1/targetmeasure-mmap>.

## Appendix A: Supplementary Algorithms

Below we provide two key algorithms from the literature we have utilized for our numerical experiments. Algorithm 2 is the pseudocode for the procedure used to select the bandwidth  $\varepsilon$  in `tm-mmap`. Algorithm 3 is the pseudocode used to obtain a quasi-uniform subsampling of the data in the numerical experiments of Section IV.

---

### Algorithm 2: Kernel Double Sum Test (Refs. 25–28)

---

**Input:** data  $X = \{x_i\}_{i=1}^N$ , diffusion matrices  $\{M(x_i)\}_{i=1}^N$ , target measure  $\mu$   
**Output:** bandwidth  $\varepsilon^*$

- 1 Choose a range of epsilon values  $\mathcal{E}$ , for example  $\varepsilon_i = 2^i, i = -20, -19, \dots, 9, 10$
- 2 **for**  $\varepsilon$  *in*  $\mathcal{E}$  **do**
- 3     Compute the kernel  $[K_\varepsilon]$
- 4     Compute  $\frac{\partial \log S(\varepsilon)}{\partial \log \varepsilon}$  according to (35)
- 5 **end**
- 6 Choose  $\varepsilon^* = \operatorname{argmax}_\varepsilon \frac{\partial \log S(\varepsilon)}{\partial \log \varepsilon}$ .

---



---

### Algorithm 3: Delta-net (Ref. 58)

---

**Input:** data  $X = \{x_i\}_{i=1}^N$ , spatial parameter  $\delta$   
**Output:** delta-net  $Z$

- 1 Choose initial ordering of the data set  $\{x_i\}_{i=1}^N$ .
- 2 Initialize  $\delta$ -net as  $Z = \{x_1\}$
- 3 **for**  $i = 2$  *to*  $N$  **do**
- 4     **if**  $\min_{z \in Z} d(x_i, z) > \delta$  **then**
- 5          $Z := Z \cup \{x_i\}$
- 6     **end**
- 7 **end**
- 8 (Optional) Prune the delta-net for isolated points
- 9 **for**  $z \in Z$  **do**
- 10     **if**  $\min_{z' \in Z} d(z', z) > 2\delta$  **then**
- 11          $Z := Z \setminus \{z\}$
- 12     **end**
- 13 **end**

---

## Appendix B: Convergence proof for `tm-mmap`

In the following we rigorously state and then prove the main result from Section III.A. For clarity we restate the necessary definitions from the text. We define the Mahalanobis kernel

$$k_\varepsilon(x, y) = \exp\left(\frac{(x-y)^\top (M^{-1}(x) + M^{-1}(y))(x-y)}{4\varepsilon}\right), \quad (\text{B1})$$

and define the **kernel density estimator**

$$\rho_\varepsilon(x) := \frac{1}{c_\varepsilon(x_i)} \int_{\Omega} k_\varepsilon(x, y) \rho(y) dy, \quad (\text{B2})$$

where

$$c_\varepsilon(x_i) := (2\pi\varepsilon)^{d/2} |M|^{1/2}(x_i). \quad (\text{B3})$$

Given that we wish to sample our target measure  $\mu$ , we will define the **right-normalized kernel** as

$$k_{\varepsilon, \mu}(x, y) := \frac{k_\varepsilon(x, y) (|M|^{-1/2}(y) \mu(y))^{1/2}}{\rho_\varepsilon(y)}, \quad (\text{B4})$$

and the operator

$$\mathcal{K}_{\varepsilon, \mu} f(x) := \int_{\Omega} k_{\varepsilon, \mu}(x, y) f(y) \rho(y) dy. \quad (\text{B5})$$

We then define the **left-normalized kernel operator**

$$\mathcal{P}_{\varepsilon,\mu}f(x) := \frac{\mathcal{H}_{\varepsilon,\mu}f(x)}{\mathcal{H}_{\varepsilon,\mu}\mathbf{1}(x)}, \quad (\text{B6})$$

where  $\mathbf{1}(x) \equiv 1$  for all  $x \in \Omega$ . Finally, we define the operator

$$\mathcal{L}_{\varepsilon,\mu}f(x) := \frac{1}{\varepsilon} (\mathcal{P}_{\varepsilon,\mu}f(x) - f(x)). \quad (\text{B7})$$

Our goal is to evaluate the limiting case for  $\varepsilon \rightarrow 0$

$$\lim_{\varepsilon \rightarrow 0} \mathcal{L}_{\varepsilon,\mu}f(x). \quad (\text{B8})$$

We will adopt two technical assumptions following the procedure in Ref. 16. The first one deals with the space of collective variables  $x$ :

**Assumption 1.** *The range of  $x$  comprises a  $d$ -dimensional manifold  $\Omega$  with no boundary and with metric tensor that locally coincides with the Euclidean metric tensor.*

*More specifically, there exists  $R > 0$  such that for any  $x, y \in \Omega$  with geodesic distance  $d_{\Omega}(x, y) \leq R$ , we have*

$$d_{\Omega}(x, y) = \|x - y\| \quad \forall x, y \in \Omega \text{ such that } d_{\Omega}(x, y) \leq R. \quad (\text{B9})$$

*In other words, the geodesic distance coincides with the Euclidean distance for any two points in  $\Omega$  provided that the geodesic distance between these points does not exceed a fixed positive number  $R$ . Moreover, we assume that given a point  $x \in \Omega$ , we can introduce a coordinate system with the origin at  $x$  and cut  $\Omega$  in such a way that the cut manifold  $\tilde{\Omega}$  is the direct product*

$$\tilde{\Omega} = [-R, R]^k \times \mathbb{R}^{d-k} \quad \text{for some } k \in \{0, 1, \dots, d\}. \quad (\text{B10})$$

The second assumption imposes integrability and smoothness conditions on the diffusion matrix  $M(x)$  and a class of functions  $f : \Omega \rightarrow \mathbb{R}$  to which we apply the constructed family of operators.

**Assumption 2.** • *The diffusion matrix  $M(x)$  is symmetric positive definite. Its inverse  $M^{-1}(x)$  is a four-times continuously differentiable matrix-valued function  $M^{-1} : \Omega \rightarrow \mathbb{R}^{d \times d}$  and the determinant of  $M^{-1}(x)$  is bounded away from zero. If the manifold  $\Omega$  is unbounded, then the entries  $(M^{-1})_{ij}(x)$  and their first derivatives  $\frac{\partial (M^{-1})_{ij}(x)}{\partial x_{\ell}}$  grow not faster than a polynomial as  $\|x\| \rightarrow \infty$ .*

• *The function  $f(x)$  is four-times continuously differentiable. If  $\Omega$  is unbounded then  $f(x)$  grows not faster than a polynomial as  $\|x\| \rightarrow \infty$ .*

Growth not faster than a polynomial is defined as follows:

**Definition.** *We say that a continuous function  $f : \mathbb{R}^d \rightarrow \mathbb{R}$  grows not faster than a polynomial as  $\|x\| \rightarrow \infty$  if there exist constants  $A \geq 0$ ,  $B \geq 0$ , and  $k \in \mathbb{N}$  such that*

$$|f(x)| \leq A + B\|x\|^k \quad \forall x \in \mathbb{R}^d.$$

**Notation.** *The notation  $\nabla \cdot M(x)$  denotes a column vector whose  $i$ th component is*

$$[\nabla \cdot M(x)]_i = \sum_{j=1}^d \frac{\partial M_{ij}(x)}{\partial x_j} \quad 1 \leq i \leq d,$$

so that  $[\nabla \cdot M(x)]_i$  is the divergence of the  $i$ th row of  $M$ .

**Theorem 1.** *Suppose a manifold  $\Omega$  and a diffusion matrix  $M(x) : \Omega \rightarrow \mathbb{R}^{d \times d}$  satisfy assumptions 1 and 2 respectively. Further, suppose we have a function  $\mu : \Omega \rightarrow \mathbb{R}$  with  $\mu \geq 0$ ,  $\int_{\Omega} \mu dx < \infty$  which satisfies Assumption 2, is absolutely continuous with respect to the sampling density  $\rho(x)$ , and which takes the form of a Gibbs measure  $\mu(x) = e^{-\beta F(x)}$  where  $F$  denotes the free energy and  $\beta^{-1}$  denotes the temperature. Let the operator  $\mathcal{L}_{\varepsilon,\mu}$  be constructed according to (B2), (B4), (B5), (B6), and (B7). Then the limit (B8) reduces to*

$$\lim_{\varepsilon \rightarrow 0} \mathcal{L}_{\varepsilon,\mu}f(x) = \frac{\beta}{2} \mathcal{L}f(x) \quad \forall x \in \Omega, \quad (\text{B11})$$

where

$$\mathcal{L}f = (-M\nabla F + \beta^{-1}(\nabla \cdot M))^{\top} \nabla f + \beta^{-1} \text{tr}[M\nabla \nabla f] \quad (\text{B12})$$

is the generator for the SDE

$$dx_t = [-M(x_t)\nabla F(x_t) + \beta^{-1}\nabla \cdot M(x_t)]dt + \sqrt{2\beta^{-1}M^{1/2}(x_t)}dw_t. \quad (\text{B13})$$

The following technical lemma established in Ref. 16 is essential for proving Theorem 1:

**Lemma 2.** *Let  $G_{\varepsilon}$  be an integral operator defined by*

$$G_{\varepsilon}f(x) = \int_{\mathbb{R}^d} e^{-\frac{1}{4\varepsilon}(x-y)^{\top}[M^{-1}(x)+M^{-1}(y)](x-y)} f(y)dy, \quad (\text{B14})$$

where the matrix function  $M$  and the scalar function  $f$  satisfy Assumption 2. Using Taylor expansions,

$$M^{-1}(y) = M^{-1}(x) + \nabla M^{-1}(x)(y-x) + r_2(x; y-x) + r_3(x; y-x) + O(\|y-x\|^4), \quad (\text{B15})$$

where  $\nabla M^{-1}(x)(y-x)$  is a matrix with entries

$$(\nabla M^{-1}(x)(y-x))_{ij} = [\nabla M_{ij}^{-1}(x)]^{\top}(y-x),$$

and  $r_2(x; z)$  and  $r_3(x; z)$  are the matrices whose entries are the second and third-order terms in Taylor expansions of  $M_{ij}^{-1}$ . Then

$$G_{\varepsilon}f(x) = c_{\varepsilon}(x) \left( f(x) + \varepsilon \left[ -\nabla f(x)^{\top} \omega_1(x) - f(x) \omega_2(x) + \frac{1}{2} \text{tr}(M(x)H(x)) \right] + O(\varepsilon^2) \right), \quad (\text{B16})$$

where  $H(x) := \nabla \nabla f(x)$  is the Hessian matrix for  $f$  evaluated at  $x$ , and for  $1 \leq i \leq d$ :

$$\omega_{1,i}(x) := \frac{1}{4\varepsilon^2 c_\varepsilon(x)} \int_{\mathbb{R}^d} e^{-\frac{z^\top M^{-1} z}{2\varepsilon}} z_i \left[ z^\top [\nabla M^{-1}(x) z] z \right] dz \quad (\text{B17})$$

$$\omega_2(x) := \frac{1}{4\varepsilon^2 c_\varepsilon(x)} \int_{\mathbb{R}^d} e^{-\frac{z^\top M^{-1} z}{2\varepsilon}} \left[ \frac{z^\top r_2(x; z) z}{4\varepsilon^2} - \frac{(z^\top [\nabla M^{-1}(x) z] z)^2}{32\varepsilon^3} \right] dz. \quad (\text{B18})$$

*Proof of Theorem 1.* With Assumptions 1 and 2 satisfied, it is sufficient to carry out the proof for  $\Omega = \mathbb{R}^d$ . Thus, all calculations below will be for the case  $\Omega = \mathbb{R}^d$ . For more details we refer to the proof of Theorem 3.2 in Ref. 16.

We first simplify the term  $\omega_1(x)$ : equation (C-54) of Ref. 16 gives

$$\nabla f^\top \omega_1 = -\frac{1}{2} \sum_{i,k=1}^d \frac{\partial M_{ik}}{\partial x_k} \frac{\partial f}{\partial x_i} + \frac{1}{4} \sum_{i,k=1}^d M_{ik} \text{tr} R_k \frac{\partial f}{\partial x_i}, \quad (\text{B19})$$

where  $\text{tr} R_k$  is given by equation (C-43) of Ref. 16 as

$$\text{tr} R_k = |M| \frac{\partial |M^{-1}|}{\partial x_k}. \quad (\text{B20})$$

Thus, using that  $|M(x)| > 0$  we can write

$$\text{tr} R_k := \frac{\partial \log |M^{-1}|}{\partial x_k}$$

and write

$$\nabla f^\top \omega_1(x) = \frac{1}{4} \sum_{i,k=1}^d M_{ik} \frac{\partial \log |M^{-1}|}{\partial x_k} \frac{\partial f}{\partial x_i} - \frac{1}{2} \sum_{i,k=1}^d \frac{\partial M_{ik}}{\partial x_k} \frac{\partial f}{\partial x_i},$$

which implies that

$$\begin{aligned} \omega_1(x) &= \frac{1}{4} M \nabla \log |M^{-1}|(x) - \frac{1}{2} \nabla \cdot M(x) \\ &= \frac{1}{2} \left( M \nabla \log |M^{-1/2}|(x) - \nabla \cdot M(x) \right). \end{aligned}$$

Thus, we can write the expansion of  $G_\varepsilon f(x)$  in  $\varepsilon$  as

$$G_\varepsilon f(x) = c_\varepsilon(x_i) (f(x) + \varepsilon Q f(x) + \mathcal{O}(\varepsilon^2)), \quad (\text{B21})$$

where the first order terms in  $\varepsilon$  are collected in the operator  $Q$  defined by

$$Q f(x) = -\nabla f(x)^\top \omega_1(x) - f(x) \omega_2(x) + \frac{1}{2} \text{tr}(M(x) \nabla \nabla f(x))$$

which can be written as

$$\begin{aligned} Q f(x) &= -\omega_2(x) f(x) \\ &+ \frac{1}{2} \left[ \left( M \nabla \log |M^{1/2}|(x) + \nabla \cdot M(x) \right)^\top \nabla f \right] \\ &+ \text{tr} \left( M(x) \nabla \nabla f(x) \right). \end{aligned} \quad (\text{B22})$$

To compute the Taylor expansion of the kernel  $\mathcal{L}_{\varepsilon, \mu}(x)$  of (B8), we will need the Taylor expansion of  $\rho_\varepsilon^{-1}(x)$  in  $\varepsilon$ . We note that a function of form  $h(\varepsilon) = (1 + C\varepsilon + \mathcal{O}(\varepsilon^2))^{-1}$  where  $C$  is a constant has the Taylor expansion  $h(\varepsilon) = 1 - \alpha C\varepsilon + \mathcal{O}(\varepsilon^2)$  at  $\varepsilon = 0$ . In our case, for fixed  $x$  the order  $\varepsilon$  term  $Q f(x)$  can be treated as a constant. From Lemma 2 and (B21), factoring out  $\rho(x)$  we can write

$$\rho_\varepsilon(x) = \rho(x) \left( 1 + \varepsilon \frac{Q \rho(x)}{\rho(x)} + \mathcal{O}(\varepsilon^2) \right) \quad (\text{B23})$$

and hence we can say that

$$\rho_\varepsilon^{-1}(x) = \rho^{-1}(x) \left( 1 - \varepsilon \frac{Q \rho(x)}{\rho(x)} + \mathcal{O}(\varepsilon^2) \right). \quad (\text{B24})$$

We now proceed to derive an asymptotic expansion of  $\mathcal{P}_{\varepsilon, \mu} f(x)$  in  $\varepsilon$ . To do so, we first introduce the following simplifying notation:

**Notation.** Given the target measure  $\mu$  and diffusion tensor  $M(x)$  with determinant  $|M(x)|$ , we define

$$\tilde{\mu}(x) := |M^{-1/2}(x)| \mu(x).$$

Then, the numerator of the left normalized kernel  $\mathcal{P}_{\varepsilon, \mu}$  from (B6) can be written as

$$\mathcal{H}_{\varepsilon, \mu} f(x) := \int_{\mathbb{R}^d} k_\varepsilon(x, y) f(y) \tilde{\mu}^{1/2}(y) \frac{\rho(y)}{\rho_\varepsilon(y)} dy. \quad (\text{B25})$$

From equation (B24) we calculate

$$\frac{\rho(y)}{\rho_\varepsilon(y)} = \left( 1 - \varepsilon \frac{Q \rho(y)}{\rho(y)} + \mathcal{O}(\varepsilon^2) \right). \quad (\text{B26})$$

Thus, plugging equation (B26) into the integrand of equation (B25), utilizing Lemma 2 and collecting higher order terms of  $\varepsilon$  we get:

$$\begin{aligned} \mathcal{H}_{\varepsilon, \mu} f(x) &= \int_{\mathbb{R}^d} \left[ k_\varepsilon(x, y) f(y) \tilde{\mu}^{1/2}(y) \right. \\ &\quad \left. \left( 1 - \varepsilon \frac{Q \rho(y)}{\rho(y)} + \mathcal{O}(\varepsilon^2) \right) \right] dy. \end{aligned} \quad (\text{B27})$$

Following (B27) and using the kernel expansion (B21),

$$\begin{aligned} \mathcal{H}_{\varepsilon, \mu} f(x) &= \int_{\mathbb{R}^d} \left[ k_\varepsilon(x, y) f(y) \tilde{\mu}^{1/2}(y) \left( 1 - \varepsilon \frac{Q \rho(y)}{\rho(y)} \right) \right] dy \\ &= c_\varepsilon \left[ f \tilde{\mu}^{1/2} + \varepsilon \left( Q(f \tilde{\mu}^{1/2}) - f \tilde{\mu}^{1/2} \frac{Q \rho}{\rho} \right) + \mathcal{O}(\varepsilon^2) \right]. \end{aligned} \quad (\text{B28})$$

Similarly,

$$\begin{aligned} \mathcal{H}_{\varepsilon, \mu} \mathbf{1}(x) &= \int_{\mathbb{R}^d} \left[ k_\varepsilon(x, y) \tilde{\mu}^{1/2}(y) \left( 1 - \varepsilon \frac{Q \rho(y)}{\rho(y)} \right) \right] dy \\ &= c_\varepsilon \left[ \tilde{\mu}^{1/2} + \varepsilon \left( Q(\tilde{\mu}^{1/2}) - \tilde{\mu}^{1/2} \frac{Q \rho}{\rho} \right) + \mathcal{O}(\varepsilon^2) \right]. \end{aligned} \quad (\text{B29})$$



For brevity in notation, we will omit the argument in  $x$  from the remainder of the proof. Collecting powers of  $\varepsilon$ , we derive the operator  $\mathcal{P}_{\varepsilon,\mu}$  from (B6) as

$$\begin{aligned}\mathcal{P}_{\varepsilon,\mu}f &= \frac{f\tilde{\mu}^{1/2} + \varepsilon \left( Q(f\tilde{\mu}^{1/2}) - f\tilde{\mu}^{1/2} \frac{Q\rho}{\rho} \right) + \mathcal{O}(\varepsilon^2)}{\tilde{\mu}^{1/2} + \varepsilon \left( Q(\tilde{\mu}^{1/2}) - \tilde{\mu}^{1/2} \frac{Q\rho}{\rho} \right) + \mathcal{O}(\varepsilon^2)} \\ &= \frac{f + \varepsilon \left( \frac{Q(f\tilde{\mu}^{1/2})}{\tilde{\mu}^{1/2}} - f \frac{Q\rho}{\rho} \right) + \mathcal{O}(\varepsilon^2)}{1 + \varepsilon \left( \frac{Q(\tilde{\mu}^{1/2})}{\tilde{\mu}^{1/2}} - \frac{Q\rho}{\rho} \right) + \mathcal{O}(\varepsilon^2)} \\ &= f + \varepsilon \left( \frac{Q(f\tilde{\mu}^{1/2})}{\tilde{\mu}^{1/2}} - f \frac{Q(\tilde{\mu}^{1/2})}{\tilde{\mu}^{1/2}} \right) + \mathcal{O}(\varepsilon^2). \quad (\text{B30})\end{aligned}$$

The Taylor expansion of  $h(\varepsilon) = (1 + C\varepsilon + \mathcal{O}(\varepsilon^2))^{-1}$  was utilized in the last step of this derivation.

We now must simplify the order  $\varepsilon$  term in (B30) using the definition of the operator  $Q$  from (B22). To expand this we note that for twice differentiable functions  $g, h$  on  $\mathbb{R}^d$ , using the chain rule and that  $M$  is symmetric we can say that

$$\begin{aligned}\text{tr}(M\nabla\nabla(gh)) &= \sum_{ij} M_{ij} \frac{\partial^2(gh)}{\partial x_i \partial x_j} \\ &= g \text{tr}(M\nabla\nabla h) + h \text{tr}(M\nabla\nabla g) \\ &\quad + 2\nabla g^\top M \nabla h. \quad (\text{B31})\end{aligned}$$

Thus,

$$\begin{aligned}Q(gh) &= -\omega_2 gh + \frac{1}{2} (h\nabla g + g\nabla h)^\top \left( M\nabla \log |M|^{1/2} + \nabla \cdot M \right) \\ &\quad + \frac{1}{2} \left( g \text{tr}(M\nabla\nabla h) + h \text{tr}(M\nabla\nabla g) \right) \\ &\quad + \nabla g^\top M \nabla h, \quad (\text{B32})\end{aligned}$$

and following the form of the order  $\varepsilon$  term of (B30) we can combine and cancel the term containing  $\omega_2$ :

$$\begin{aligned}\frac{Q(gh)}{h} - g \frac{Q(h)}{h} &= \frac{1}{2} \left( M\nabla \log |M|^{1/2} + \nabla \cdot M \right)^\top \nabla g \\ &\quad + \frac{\nabla g^\top M \nabla h}{h} + \frac{1}{2} \text{tr}(M\nabla\nabla g) \\ &= \frac{1}{2} \left[ \left( M\nabla \log |M|^{1/2} + 2M \frac{\nabla h}{h} + \nabla \cdot M \right)^\top \nabla g \right. \\ &\quad \left. + \text{tr}(M\nabla\nabla g) \right].\end{aligned}$$

Substituting  $g = f$  and  $h = \tilde{\mu}^{1/2}$  into the last expression and

plugging it into (B30) we obtain:

$$\begin{aligned}(\mathcal{P}_{\varepsilon,\mu}f - f)(x) &= \frac{\varepsilon}{2} \left[ \left( M\nabla \log |M|^{1/2} + 2M\nabla \log(\tilde{\mu}^{1/2}) + \nabla \cdot M \right)^\top \nabla f \right. \\ &\quad \left. + \text{tr}(M\nabla\nabla f) \right] + \mathcal{O}(\varepsilon^2) \\ &= \frac{\varepsilon}{2} \left[ \left( M\nabla \log \mu + \nabla \cdot M \right)^\top \nabla f \right. \\ &\quad \left. + \text{tr}(M\nabla\nabla f) \right] + \mathcal{O}(\varepsilon^2). \quad (\text{B33})\end{aligned}$$

Therefore, for  $\mu(x) = e^{-\beta F(x)}$ , the operator  $\mathcal{L}_{\varepsilon,\mu}$  is:

$$\begin{aligned}\mathcal{L}_{\varepsilon,\mu}f(x) &= \frac{1}{\varepsilon} (\mathcal{P}_{\varepsilon,\mu}f - f)(x) \\ &= \frac{\beta}{2} \left[ \left( -M\nabla F(x) + \nabla \cdot M \right)^\top \nabla f \right. \\ &\quad \left. + \beta^{-1} \text{tr}(M\nabla\nabla f) \right] + \mathcal{O}(\varepsilon) \\ &= \frac{\beta}{2} \mathcal{L}f + \mathcal{O}(\varepsilon). \quad (\text{B34})\end{aligned}$$

Thus, taking the limit as  $\varepsilon \rightarrow 0$  we obtain the desired result:

$$\lim_{\varepsilon \rightarrow 0} \mathcal{L}_{\varepsilon,\mu}f(x) = \frac{\beta}{2} \mathcal{L}f. \quad (\text{B35})$$

□

- <sup>1</sup>W. E and E. Vanden-Eijnden, in *Multiscale modelling and simulation* (Springer, 2004) pp. 35–68.
- <sup>2</sup>W. E and E. Vanden-Eijnden, *Journal of statistical physics* **123**, 503 (2006).
- <sup>3</sup>W. E and E. Vanden-Eijnden, *Annual Review of Physical Chemistry* **61**, 391 (2010), pMID: 18999998, <https://doi.org/10.1146/annurev.physchem.040808.090412>.
- <sup>4</sup>R. Satija, A. M. Berezhkovskii, and D. E. Makarov, *Proceedings of the National Academy of Sciences* **117**, 27116 (2020).
- <sup>5</sup>M. Cameron, *Journal of Computational Physics* **247**, 137 (2013).
- <sup>6</sup>L. Maragliano, A. Fischer, E. Vanden-Eijnden, and G. Ciccotti, *The Journal of chemical physics* **125**, 024106 (2006).
- <sup>7</sup>P. Ravindra, Z. Smith, and P. Tiwary, *Molecular Systems Design & Engineering* **5**, 339 (2020).
- <sup>8</sup>M. A. Rohrdanz, W. Zheng, M. Maggioni, and C. Clementi, *The Journal of chemical physics* **134**, 03B624 (2011).
- <sup>9</sup>S. Piana and A. Laio, *Physical review letters* **101**, 208101 (2008).
- <sup>10</sup>F. Sittel and G. Stock, *The Journal of chemical physics* **149**, 150901 (2018).
- <sup>11</sup>G. M. Rotskoff and E. Vanden-Eijnden, arXiv preprint arXiv:2008.06334 (2020).
- <sup>12</sup>H. Li, Y. Khoo, Y. Ren, and L. Ying, *Proceedings of Machine Learning Research* vol **107**, 1 (2021).
- <sup>13</sup>Q. Li, B. Lin, and W. Ren, *The Journal of Chemical Physics* **151**, 054112 (2019).
- <sup>14</sup>Y. Khoo, J. Lu, and L. Ying, *Research in the Mathematical Sciences* **6**, 1 (2019).
- <sup>15</sup>Z. Trstanova, B. Leimkuhler, and T. Lelièvre, *Proceedings of the Royal Society A* **476**, 20190036 (2020).
- <sup>16</sup>L. Evans, M. K. Cameron, and P. Tiwary, arXiv preprint arXiv:2108.08979 (2021).
- <sup>17</sup>R. R. Coifman and S. Lafon, *Applied and computational harmonic analysis* **21**, 5 (2006).

- <sup>18</sup>A. Singer and R. R. Coifman, *Applied and Computational Harmonic Analysis* **25**, 226 (2008).
- <sup>19</sup>A. L. Ferguson, A. Z. Panagiotopoulos, P. G. Debenedetti, and I. G. Kevrekidis, *The Journal of chemical physics* **134**, 04B606 (2011).
- <sup>20</sup>T. Berry and T. Sauer, *Applied and Computational Harmonic Analysis* **40**, 439 (2016).
- <sup>21</sup>R. Banisch, Z. Trstanova, A. Bittracher, S. Klus, and P. Koltai, *Applied and Computational Harmonic Analysis* **48**, 242 (2020).
- <sup>22</sup>G. M. Torrie and J. P. Valleau, *Journal of Computational Physics* **23**, 187 (1977).
- <sup>23</sup>A. Laio and M. Parrinello, *Proceedings of the National Academy of Sciences* **99**, 12562 (2002).
- <sup>24</sup>G. J. Moro and F. Cardin, *Chemical physics* **235**, 189 (1998).
- <sup>25</sup>T. Berry, D. Giannakis, and J. Harlim, *Physical Review E* **91**, 032915 (2015).
- <sup>26</sup>T. Berry and J. Harlim, *Applied and Computational Harmonic Analysis* **40**, 68 (2016).
- <sup>27</sup>D. Giannakis, *Applied and Computational Harmonic Analysis* **47**, 338 (2019).
- <sup>28</sup>A. D. Davis and D. Giannakis, arXiv preprint arXiv:2104.15124 (2021).
- <sup>29</sup>B. P. Vani, J. Weare, and A. Dinner, *The Journal of Chemical Physics* (2022).
- <sup>30</sup>G. A. Pavliotis, **60** (2014).
- <sup>31</sup>J. E. Straub, M. Borkovec, and B. J. Berne, *Journal of Physical Chemistry* **91**, 4995 (1987).
- <sup>32</sup>E. Carter, G. Ciccotti, J. T. Hynes, and R. Kapral, *Chemical Physics Letters* **156**, 472 (1989).
- <sup>33</sup>J. G. Kirkwood, *The Journal of chemical physics* **3**, 300 (1935).
- <sup>34</sup>A. Ma, A. Nag, and A. R. Dinner, *The Journal of chemical physics* **124**, 144911 (2006).
- <sup>35</sup>B. Peters, *Annual review of physical chemistry* **67**, 669 (2016).
- <sup>36</sup>P. L. Geissler, C. Dellago, and D. Chandler, *The Journal of Physical Chemistry B* **103**, 3706 (1999).
- <sup>37</sup>U. Von Luxburg, *Statistics and computing* **17**, 395 (2007).
- <sup>38</sup>M. Belkin and P. Niyogi, *Neural computation* **15**, 1373 (2003).
- <sup>39</sup>S.-T. Tsai and P. Tiwary, *Molecular Simulation* **47**, 449 (2021).
- <sup>40</sup>L. Boninsegna, G. Gobbo, F. Noé, and C. Clementi, *Journal of chemical theory and computation* **11**, 5947 (2015).
- <sup>41</sup>A. L. Ferguson, A. Z. Panagiotopoulos, P. G. Debenedetti, and I. G. Kevrekidis, *Proceedings of the National Academy of Sciences* **107**, 13597 (2010).
- <sup>42</sup>W. Zheng, M. A. Rohrdanz, M. Maggioni, and C. Clementi, *The Journal of chemical physics* **134**, 144109 (2011).
- <sup>43</sup>R. R. Coifman, I. G. Kevrekidis, S. Lafon, M. Maggioni, and B. Nadler, *Multiscale Modeling & Simulation* **7**, 842 (2008).
- <sup>44</sup>Q. Tan, M. Duan, M. Li, L. Han, and S. Huo, *The Journal of chemical physics* **151**, 105101 (2019).
- <sup>45</sup>S.-T. Tsai, Z. Smith, and P. Tiwary, *Journal of Chemical Theory and Computation* **17**, 6757 (2021).
- <sup>46</sup>M. R. Soresen and A. F. Voter, *The Journal of Chemical Physics* **112**, 9599 (2000).
- <sup>47</sup>C. F. Abrams and E. Vanden-Eijnden, *Proceedings of the National Academy of Sciences* **107**, 4961 (2010).
- <sup>48</sup>J. Wang, P. Cieplak, and P. A. Kollman, *Journal of computational chemistry* **21**, 1049 (2000).
- <sup>49</sup>H. A. Kramers, *Physica* **7**, 284 (1940).
- <sup>50</sup>M. E. Johnson and G. Hummer, *The Journal of Physical Chemistry B* **116**, 8573 (2012).
- <sup>51</sup>R. B. Best and G. Hummer, *Proceedings of the National Academy of Sciences* **107**, 1088 (2010).
- <sup>52</sup>F. Sicard, V. Koskin, A. Annibale, and E. Rosta, *Journal of Chemical Theory and Computation* **17**, 2022 (2021).
- <sup>53</sup>O. Lindenbaum, M. Salhov, A. Yeredor, and A. Averbuch, *Data mining and knowledge discovery* **34**, 1676 (2020).
- <sup>54</sup>A. Barducci, G. Bussi, and M. Parrinello, *Phys. Rev. Lett.* **100**, 020603 (2008).
- <sup>55</sup>O. Valsson, P. Tiwary, and M. Parrinello, *Annual review of physical chemistry* **67**, 159 (2016).
- <sup>56</sup>J. F. Dama, M. Parrinello, and G. A. Voth, *Physical review letters* **112**, 240602 (2014).
- <sup>57</sup>P. Tiwary and M. Parrinello, *The Journal of Physical Chemistry B* **119**, 736 (2015).
- <sup>58</sup>M. Crosskey and M. Maggioni, *Multiscale Modeling & Simulation* **15**, 110 (2017).
- <sup>59</sup>G. A. Tribello, M. Bonomi, D. Branduardi, C. Camilloni, and G. Bussi, *Comput. Phys. Commun.* **185**, 604 (2014).
- <sup>60</sup>T. Gao, *Applied and Computational Harmonic Analysis* **50**, 147 (2021).
- <sup>61</sup>D. Van Der Spoel, E. Lindahl, B. Hess, G. Groenhof, A. E. Mark, and H. J. Berendsen, *Journal of computational chemistry* **26**, 1701 (2005).
- <sup>62</sup>P. G. Bolhuis, C. Dellago, and D. Chandler, *Proceedings of the National Academy of Sciences* **97**, 5877 (2000).
- <sup>63</sup>P. Tiwary and M. Parrinello, *Physical review letters* **111**, 230602 (2013).
- <sup>64</sup>S. Mehdi and P. Tiwary, "Thermodynamics of interpretation," (2022).
- <sup>65</sup>D. Branduardi, G. Bussi, and M. Parrinello, *Journal of chemical theory and computation* **8**, 2247 (2012).
- <sup>66</sup>F. Nüske, P. Koltai, L. Boninsegna, and C. Clementi, *Entropy* **23**, 134 (2021).
- <sup>67</sup>L. Maragliano, B. Roux, and E. Vanden-Eijnden, *Journal of chemical theory and computation* **10**, 524 (2014).
- <sup>68</sup>B. Roux, *The Journal of Physical Chemistry A* **125**, 7558 (2021).
- <sup>69</sup>D. Kushnir, A. Haddad, and R. R. Coifman, *Applied and Computational Harmonic Analysis* **32**, 280 (2012).
- <sup>70</sup><https://github.com/DiffusionMapsAcademics/pyDiffMap>.